

Case History

Multiparameter full-waveform inversion of 3D ocean-bottom cable data from the Valhall field

Nishant Kamath¹, Romain Brossier², Ludovic Métivier³, Arnaud Pladys², and Pengliang Yang²

ABSTRACT

Full-waveform inversion (FWI) applications on 3D ocean-bottom cable (OBC) data from the Valhall oil field in the North Sea have demonstrated the importance of appropriately accounting for attenuation. The Valhall field contains unconsolidated shallow sediments and a low-velocity anomaly in its center — indicative of gas clouds — which have a significant attenuation imprint on the data. Our challenge is to perform time-domain viscoacoustic 3D FWI, which requires more sophisticated tools than in the frequency domain wherein attenuation can be incorporated in a straightforward manner. The benefit of using a viscoacoustic, instead of a purely acoustic,

modeling engine is illustrated. We have determined that, in the frequency band used (2.5–7.0 Hz), it is better to reconstruct the velocity only keeping the attenuation fixed because simultaneous inversion of the velocity and quality factor Q does not provide reliable Q updates. We develop an efficient time-domain workflow combining a random source decimation algorithm, modeling using standard linear solid mechanisms, and wavefield preconditioning. Our results are similar to those obtained from state-of-the-art frequency-domain algorithms, at a lower computational cost compared to conventional checkpointing techniques. We clearly illustrate the improvement in terms of imaging and data fit achieved when accounting for attenuation.

INTRODUCTION

Several case studies have proven full-waveform inversion (FWI) to be a valuable tool in estimating high-resolution models of mechanical properties of the subsurface (Pratt and Shipp, 1999; Plessix and Perkins, 2010; Raknes et al., 2015; Górszczyk et al., 2017). Previous work in the North Sea, for example, by Warner et al. (2013) and Haacke et al. (2019), addresses issues related to reconstructing velocity of the subsurface, where the sediments are known to be gas bearing and, hence, viscous. To circumvent the problem of explicitly including attenuation in the modeling engine, preprocessing can be applied to the observed and modeled data. Warner et al. (2013) equalize the root-mean square (rms) amplitudes of the observed data and normalize the modeled data within a broad sliding

time window as part of their data processing to invert 3D ocean-bottom cable (OBC) data from the Tommeliten Alpha field in the North Sea. Haacke et al. (2019) invert ocean bottom node and towed-streamer data from the South Arne field in the Danish North Sea simultaneously to obtain the velocity V_{P0} , anisotropy coefficient ϵ , and quality factor Q .

The first FWI study of a data set from Valhall was performed by Sirgue et al. (2010) to address the challenge of imaging the crest of the reservoir, obscured by the presence of gas-bearing sediments in the overburden. They run isotropic FWI in the frequency domain by converting an initial anisotropic velocity to an “equivalent isotropic” one. The inverted velocity yielded images that were superior to those obtained from tomography.

Manuscript received by the Editor 2 November 2019; revised manuscript received 15 August 2020; published ahead of production 4 October 2020; published online 20 January 2021.

¹University of Grenoble Alpes, ISTerre, Grenoble, 38400, France; currently at CGG, Crawley, UK. E-mail: geo.nishant@gmail.com (corresponding author).

²University of Grenoble Alpes, ISTerre, Grenoble, 38400, France. E-mail: romain.brossier@univ-grenoble-alpes.fr; arnaud.pladys@univ-grenoble-alpes.fr; ypl.2100@gmail.com.

³University of Grenoble Alpes, ISTerre, Grenoble, 38400, France and University of Grenoble Alpes, CNRS, LJK, Grenoble, 38041, France. E-mail: ludovic.metivier@univ-grenoble-alpes.fr.

© 2021 Society of Exploration Geophysicists. All rights reserved.

Prieux et al. (2013) invert a 2D line of hydrophone data (OBC) from the Valhall field for P-wave vertical velocity V_{P0} , density, and attenuation, in the frequency domain, with the medium assumed to be transversely isotropic with a vertical symmetry axis (VTI). They recommend a hierarchical approach, wherein the velocity is updated first, followed by joint inversion of all three parameters (V_P , ρ , and Q). Radiation patterns for perturbations in velocity and anisotropy parameters in VTI media are analyzed by Gholami et al. (2013). The accuracy and resolution of the reconstructed P-wave vertical, horizontal, or normal moveout velocity are found to be fairly similar if the low-wavenumber components of the anisotropy fields are correct. They test this on the same 2D data used by Prieux et al. (2013).

The same data set in its entirety (i.e., the 3D data set) is inverted by Operto et al. (2015) in the frequency domain. They model the wavefield assuming the medium is VTI, and they reconstruct the P-wave vertical velocity V_{P0} , keeping the anisotropy coefficients ϵ and δ as well as the density and attenuation fixed at their initial values during inversion. They assert that running monofrequency (discrete frequencies from 3.5 to 10.0 Hz) FWI is more conducive to reducing the imprint of inaccuracies in the attenuation field on the inversion. In their later work (Operto and Miniussi, 2018), they update V_{P0} , density ρ , and quality factor Q simultaneously in the frequency domain by inverting groups of discrete frequencies. Apparently, the grouping of frequencies helps to better model the dispersive part of the wavefield, leading to more reliable updates in the parameters. In addition, the data redundancy helps mitigate trade-offs between the reconstructed parameters. They show that the acquisition footprint in the reconstructed velocity field is severely mitigated because these artifacts are partially absorbed by the parameters ρ and Q .

The objective of the present study is to design a suitable time-domain viscoacoustic FWI workflow to invert exploration-scale data acquired in a region where the presence of gas raises specific imaging challenges. We focus on the time-domain approach because of its greater flexibility and scalability compared to the frequency domain, which makes it more amenable to handling large-scale 3D case studies. We highlight the importance of taking attenuation into account, as opposed to assuming the medium to be purely acoustic. We are also interested in reconstructing the quality factor

Q along with the P-wave vertical velocity V_{P0} because time-domain modeling is more amenable to the simultaneous updating of velocity and Q (Operto and Miniussi, 2018).

In the first section, “Data and initial models,” we describe the geology of the Valhall field and the data set used in the study. The theory of modeling viscoacoustic wavefield in VTI media in the time domain, and the inversion strategy adopted to perform FWI, are explained in the second section, “Modeling and inversion methodology.” We elaborate on the preprocessing of the hydrophone component used in the inversion, as well as of the estimation of the source-time function from the data in the third section, “Data processing and experimental set up.” The inversion results are presented in the fourth section, “FWI results.” Inversion is run for three different scenarios: (1) we update the P-wave vertical velocity V_{P0} assuming the medium is nonattenuative, (2) the V_{P0} -field is inverted in a viscoacoustic medium with constant values of quality factor Q in the subsurface, and (3) the values of the velocity and Q are updated simultaneously. We present the quality control (QC) performed on the results: evaluation of data fit, comparison of objective function, as well as that of the inversion results with available well logs, and images derived from the FWI model updates. The results are addressed in the “Discussion” section, and finally we draw conclusions from our study.

DATA AND INITIAL MODELS

The Valhall field, discovered in 1975, is located in the southern part of the Norwegian North Sea, 300 km to the southwest of Stavanger. It lies along the Lindesnes Ridge, which trends north–northwest (Munns, 1985; Leonard and Munns, 1987), and it is characterized by an Upper Cretaceous chalk reservoir at a depth of 2.4 km, overlain by gas-bearing Tertiary shale. Although the reservoir is structurally complex, the Tertiary overburden is relatively free of structure (Hall et al., 2002). The water column has a near-constant depth of approximately 70 m.

The four-component OBC data, of which we use only the hydrophone component in this study, were acquired in 2011 as part of the Valhall Life of Field Seismic project (Barkved et al., 2003). The survey consists of 50,824 shots, 5 m below the ocean surface, and 2048 receivers, each spaced 50 m apart (Figure 1). The cable spacing is 300 m, and the data are sampled at 4 ms. The survey covers an area of approximately 145 km². We apply reciprocity, and we exchange the source and receiver positions to save computational cost during FWI.

We use the same initial velocity and anisotropy models (Figure 2) as the ones used in Prieux et al. (2011), Operto et al. (2015), and Operto and Miniussi (2018), provided courtesy of BP. The models were generated by reflection traveltime tomography, and their efficacy as initial models for FWI has been studied in the abovementioned work. Prieux et al. (2011) compute the traveltimes of first arrivals in a 2D section (at approximately $x = 6.7$ km) of this model and conclude that diving waves sample depths down to 1.5 km. The model updates beneath 1.5 km can then be primarily attributed to reflected events in the data. Comparing data in the 3–7 Hz range with those generated in the initial model, Operto et al. (2015) observe that the diving waves are within half a cycle of each other, confirming that the initial velocity and anisotropy parameters can indeed be used for FWI.

We do not apply smoothing to the sharp interface at the reservoir ($z = 2.5$ km) because we expect the reflected energy to help update the part of the model not probed by the diving energy. Although structurally not complex, the anisotropy in the region is significant,

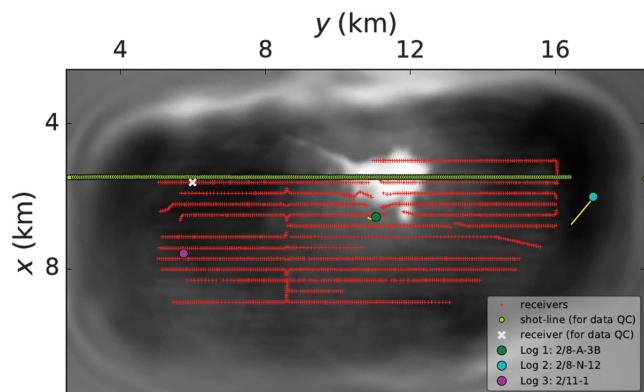


Figure 1. Locations of the receivers (red), a line of shots (green-yellow) and three well logs (magenta, green, and cyan) overlaid on a depth slice ($z = 1$ km) of the velocity reconstructed from viscoacoustic FWI. The white cross indicates the receiver at which the data along the shot line are compared subsequently. The yellow lines starting from logs 1 and 2 are projections of the respective trajectories on the horizontal plane.

with ε as high as 0.20. Density is computed from the initial velocity field using Gardner's relationship (Gardner et al., 1974), given as $\rho = 309.6(V_{p0})^{0.25}$. The initial Q model (for viscoacoustic media) has values of 1000 in the water column and 200 in the sediments. The values of Q are chosen such that they help us match the rms energy of early-arriving phases of the observed data to those generated in the initial model as shown in Prioux et al. (2011) and Operto et al. (2015).

MODELING AND INVERSION METHODOLOGY

Modeling

Frequency-domain FWI (Pratt, 1999; Brossier et al., 2009; Prioux et al., 2013; Operto et al., 2015) has certain distinct advantages: data decimation is a natural consequence of computing the wavefield for a set of discrete frequencies. Attenuation can be easily incorporated by defining a complex-valued velocity field (Kolsky, 1956; Futterman, 1962). In addition, the impedance matrix, once decomposed, can be used to generate the wavefield for all of the sources at little additional expense. To this end, parallel direct solvers, such as the multifrontal massively parallel sparse (MUMPS) solver (Amestoy et al., 2015), have been used for FWI by Operto et al. (2015) and Amestoy et al. (2016). The size of the impedance matrix, however, is proportional to the dimensions of the model which, in turn, depends on the frequency for which data are being generated. For a 3D model with dimensions $N \times N \times N$, the computational complexity of wavefield modeling is $O(N^6)$, whereas the memory complexity is $O(N^4)$ (Operto et al., 2007; Li et al., 2015). Depending on the architecture of the supercomputer and the efficiency of the parallel direct solver used, this could lead to a bottleneck in memory and/or scalability issues and render large-scale problems intractable using conventional computational resources.

Time-domain modeling, however, might require some form of more stringent data decimation (either simultaneous source-encoding or subsampling), but it benefits from much better scalability, allowing us to tackle large-scale problems with two levels of parallelization, over sources and domains, with conventional domain decomposition processes. This is because although the computational complexity of time-domain methods is similar to that of frequency-domain parallel direct solvers, the memory complexity is an order of magnitude lower, i.e., $O(N^3)$ (Li et al., 2015).

Of the various kinds of existing rheological models used to represent the behavior of viscoelastic materials, such as the Maxwell body, Kelvin–Voigt, and standard linear solid (SLS), a mechanical model consisting of a combination of SLS bodies (i.e., a generalized SLS model) has been shown to best describe the physical properties

of viscoelastic solids (Casula and Carcione, 1992). The viscoelastic wave equation for such a model can be expressed as (Yang et al., 2016b):

$$\begin{aligned} \rho \partial_t \mathbf{v} &= \nabla \cdot \boldsymbol{\sigma} \\ \partial_t \boldsymbol{\sigma} &= \mathbf{M}_u : \left(\nabla \cdot \mathbf{v} - \sum_{\ell=1}^L Y_\ell \boldsymbol{\xi}_\ell \right) \\ \partial_t \boldsymbol{\xi}_\ell + \omega_\ell \boldsymbol{\xi}_\ell &= \omega_\ell \nabla \cdot \mathbf{v}, \quad \ell = 1, 2, \dots, L, \end{aligned} \quad (1)$$

where ρ is the density, \mathbf{v} is the particle velocity, $\boldsymbol{\sigma}$ is the stress, \mathbf{M}_u is the unrelaxed modulus (i.e., the modulus as $\omega \rightarrow \infty$), “ ∇ ” is the vector differential operator, and “ \cdot ” and “ $:$ ” represent the dot product and double dot product, respectively. A combination of L attenuation mechanisms, with relaxation functions $\boldsymbol{\xi}_\ell$, along with the associated anelastic coefficients Y_ℓ , and reference frequencies ω_ℓ , simulate a constant attenuation within the frequency range of interest. In our study, $L = 3$ and the reference frequencies ω_ℓ are 1, 6.32, and 40 Hz.

The details of computing the coefficient Y_ℓ can be found in Blanch et al. (1995) and Yang et al. (2016b); here, we briefly describe how Y_ℓ is estimated. For the model represented by equation 1, the quality factor $Q(\omega)$, whose inverse is proportional to the fraction of energy lost per cycle, is related to the anelastic coefficients and reference frequencies via the equation

$$Q^{-1}(\omega) = \frac{\sum_{\ell=1}^L Y_\ell \frac{\omega_\ell \omega}{\omega_\ell^2 + \omega^2}}{1 - \sum_{\ell=1}^L Y_\ell \frac{\omega_\ell^2}{\omega_\ell^2 + \omega^2}}. \quad (2)$$

In realistic attenuative media, we can assume $Q(\omega) \gg 1$ (Blanch et al., 1995), leading to the denominator in equation 2 to be ≈ 1 . We also assume that $Q(\omega)$ can be represented by a constant value Q_0 within the frequency range of interest. The coefficients Y_ℓ can then be obtained by minimizing

$$\int_{\omega_1}^{\omega_2} \left[1 - \sum_{\ell=1}^L \left(y_\ell \frac{\omega_\ell \omega}{\omega_\ell^2 + \omega^2} \right) \right]^2, \quad (3)$$

with respect to the variable y_ℓ ($:= Q_0 Y_\ell$).

Yang et al. (2018) show that equation 1, in the acoustic approximation of VTI media (Alkhalifah, 1998; Duveneck and Bakker, 2011), simplifies as

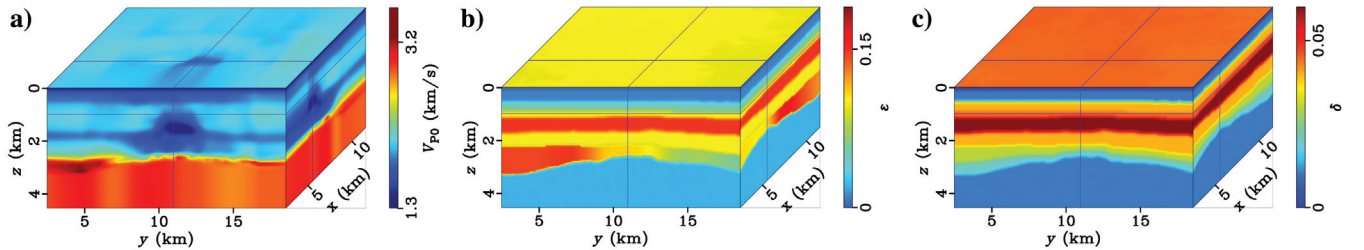


Figure 2. Initial model provided to us by Aker BP: (a) the P-wave vertical velocity V_{p0} , and the anisotropy coefficients (b) ε and (c) δ . The values along the sections inside the cubes, denoted by the lines, are projected on the respective faces.

$$\rho \partial_t v_x = \partial_x g$$

$$\rho \partial_t v_y = \partial_y g$$

$$\rho \partial_t v_z = \partial_z q$$

$$\partial_t g = c_{11}(\partial_x v_x + \partial_y v_y) + c_{13} \partial_z v_z - \sum_{\ell=1}^L Y_\ell [c_{11} \xi_\ell^g + c_{13} \xi_\ell^q]$$

$$\partial_t q = c_{13}(\partial_x v_x + \partial_y v_y) + c_{33} \partial_z v_z - \sum_{\ell=1}^L Y_\ell [c_{13} \xi_\ell^g + c_{33} \xi_\ell^q]$$

$$\partial_t \xi_\ell^g = -\omega_\ell \xi_\ell^g + \omega_\ell (\partial_x v_x + \partial_y v_y), \quad \ell = 1, 2, \dots, L$$

$$\partial_t \xi_\ell^q = -\omega_\ell \xi_\ell^q + \omega_\ell \partial_z v_z, \quad \ell = 1, 2, \dots, L, \quad (4)$$

where c_{11} , c_{33} , and c_{13} are the stiffness coefficients, $g := \sigma_{xx} = \sigma_{yy}$, $q := \sigma_{zz}$, $\xi_\ell^{xx} + \xi_\ell^{yy} := \xi_\ell^g$, and $\xi_\ell^{zz} := \xi_\ell^q$. In the acoustic approximation to VTI media, the following equations relate the stiffness coefficients to the P-wave vertical velocity V_{p0} and the anisotropy parameters ε and δ (Duvencak and Bakker, 2011; Yang et al., 2018):

$$\begin{aligned} c_{11} &= \rho V_{p0}^2 (1 + 2\varepsilon) \\ c_{33} &= \rho V_{p0}^2 \\ c_{13} &= \rho V_{p0}^2 (1 + 2\delta). \end{aligned} \quad (5)$$

In this study, we rely on a finite-difference discretization (second order in time and fourth order in space) of these equations. The free surface is modeled at $z = 0$ m, whereas absorbing (sponge) layers are used beyond the limits of the model to mimic a medium of infinite extent (Cerjan et al., 1985). Windowed sinc interpolation (Hicks, 2002) allows us to locate sources and receivers accurately on the finite-difference grid.

Note that the wavefield velocity in a viscous medium depends on the frequency. However, the P-wave vertical velocity V_{p0} in equation 5 is the velocity as $\omega \rightarrow \infty$. To obtain the apparent velocity in the frequency range of interest, we compute the so-called kinematic velocity (Hao, 2019), which corresponds to an equivalent velocity corresponding to a given peak frequency (see Appendix A).

Inversion

The inversion is set up to minimize the following least-squares objective function:

$$\chi(\mathbf{m}) := \frac{1}{2} \int_0^T \|\mathbf{d}_{\text{cal}}(\mathbf{m}) - \mathbf{d}_{\text{obs}}\|^2 dt, \quad (6)$$

where \mathbf{d}_{obs} are the observed data, $\mathbf{d}_{\text{cal}}(\mathbf{m})$ are the data generated from the model \mathbf{m} , and T is the recording time. Only the pressure data from the hydrophone are inverted in this study.

The adjoint-state method is used to compute the gradient of the objective function with respect to the model parameters (Tarantola, 1984; Plessix, 2006). Although the updates are performed for V_{p0} and Q^{-1} , the gradients are obtained with respect to κ^{-1} (where $\kappa := \rho V_{p0}^2$) and Q^{-1} according to (Yang et al., 2018)

$$\begin{aligned} \frac{\partial \chi}{\partial \kappa^{-1}} &= \frac{1}{2(\varepsilon - \delta)} \int_0^T \left\{ \left(\bar{g} - \sqrt{1 + 2\delta \bar{q}} \right) \partial_t g \right. \\ &\quad \left. + \left[-\sqrt{1 + 2\delta \bar{g}} + (1 + 2\varepsilon) \bar{q} \right] \partial_t q \right\} dt, \\ \frac{\partial \chi}{\partial Q^{-1}} &= \int_0^T \left(\bar{g} \sum_{\ell=1}^L y_\ell \xi_\ell^g + \bar{q} \sum_{\ell=1}^L y_\ell \xi_\ell^q \right) dt, \end{aligned} \quad (7)$$

where the quantities under the bar represent adjoint-state variables. These are computed by solving the wave equation backward in time, with the data residuals as the forcing functions (Plessix, 2006; Yang et al., 2018).

Gradient computation requires access to the forward and adjoint wavefields. However, for realistic 3D problems, it is often not possible to store the forward wavefield on a disk (challenging for input/output-intensive problems) or in memory (because of its size). The forward wavefield is hence recomputed along with the adjoint wavefield from the boundary values stored during the forward simulation and those at the final time step. In attenuative media, the forward wavefield, when reconstructed in reverse time, is susceptible to numerical instabilities, and checkpointing is commonly used to mitigate this problem (Griewank and Walther, 2000; Anderson et al., 2012).

The checkpoint-assisted reverse forward simulation (CARFS) strategy proposed by Yang et al. (2016c), wherein wavefield stored at checkpoints during forward simulation can be used to either forward- or back-propagate a wavefield from a given checkpoint during the reconstruction based on an energy threshold, providing a stable and yet more efficient (compared to conventional checkpointing) means of computing the gradient. In addition, the CARFS strategy is dedicated to the situation in which the manner that FWI is implemented (using openMP instead of domain decomposition) and hardware constraints allow us only a few GB of RAM per shot. When domain decomposition is used and/or high performance computing (HPC) architecture with large RAM is available, it is always more efficient to store the incident wavefield in the memory (or on fast disks). In our work, such an architecture was not available: we used a Blue Gene machine with very low RAM per node (16 GB per node and 16 cores per node).

The model is updated every iteration using a preconditioned limited-memory Broyden–Fletcher–Goldfarb–Shanno algorithm (l-BFGS) (Nocedal, 1980), as implemented in the SEISCOPE optimization toolbox (Métivier and Brossier, 2016). The wavefield preconditioner, which is a modified version of illumination compensation, is presented in Appendix B. We apply Gaussian smoothing to the gradient, with the correlation lengths being fractions (0.4 and 0.3 in the horizontal and vertical directions, respectively) of the local wavelength $\lambda(\mathbf{x})$, based on the current estimate of velocity $V_{p0}(\mathbf{x})$ and an average frequency f_{average} :

$$\lambda(\mathbf{x}) = \frac{V_{p0}(\mathbf{x})}{f_{\text{average}}}. \quad (8)$$

Reconstructed parameters

When FWI is performed in viscoacoustic media, attenuation can be a “passive parameter” (wherein the attenuation remains un-

changed during the inversion), or it can be updated (i.e., it is an “active parameter”). [Operto and Miniussi \(2018\)](#) conclude that the velocity updates from V_{P0} -only inversion (in viscoacoustic media) were consistent with those from reconstructing it simultaneously with density and attenuation. This is because the inversion below 10 Hz is dominated by the difference in phase between the modeled and observed data. Including ρ and Q as active parameters, however, reduces the acquisition footprint on the inverted velocity V_{P0} ([Operto and Miniussi, 2018](#)). We choose not to update the density by applying Gardner’s relationship to the inverted V_{P0} because errors in the velocity would propagate into ρ and possibly bias subsequent inversion. Hence, we retain the smooth density-field obtained from the initial V_{P0} (Figure 2a) throughout the inversion and update either V_{P0} only or V_{P0} and Q simultaneously. A matter of detail here is that, during the inversion, we navigate through a model space defined by parameters V_{P0} and the attenuation factor Q^{-1} . Additionally, each parameter is normalized in the optimization so that its value lies between 0 and 1. This is the strategy that was adopted by [Yang et al. \(2018\)](#).

DATA PROCESSING AND EXPERIMENTAL SET UP

The data were provided to us in the SEG Y format, with no pre-processing applied. The coordinates of the data and models are transformed from real-world to local coordinates (with the origin at $x = 0$ km and $y = 0$ km). We then apply source-receiver reciprocity to decrease the cost of inversion. This is followed by despiking the data and then application of minimum-phase band-pass filters (Figure 3) in the 2.5–5.0 Hz and 2.5–7.0 Hz frequency ranges (referred to as band 1 and band 2, respectively). The white and yellow arrows depicted in Figure 3a indicate reflections from the top of the gas and the top of the chalk, respectively, as shown by [Operto and Miniussi \(2018\)](#). The linear event with a velocity of ≈ 400 m/s, identified by the black arrow, denotes Schölte waves. We compute the energy (rms) of each gather and perform manual QC of gathers with large amplitudes.

The grid spacing of the models for the first and second frequency bands are set to 70 and 50 m, respectively, to ensure five grid points for the smallest wavelength. The frequency ranges (for the two bands) and the grid spacing of the models are similar to those chosen by [Operto et al. \(2015\)](#).

At the beginning of the run for each frequency band, we estimate the source-time function by solving a linear inverse problem ([Pratt,](#)

[1999](#)). A random selection of 128 gathers is used for the source inversion, and it is performed using the updated velocity and attenuation models (where applicable).

It is important to apply appropriate weights to the data during source estimation. The initial velocity model allows us to predict the reflection only from the top of the chalk. Without any time windowing, the inverted (erroneous) wavelet would account for all reflected events. In addition, the observed data contain Schölte waves, which cannot be generated when the wavefield is modeled in the acoustic approximation. Hence, we apply an inner mute to ensure that only the direct arrivals are used for computing the wavelet (Figure 4a). There are also differences in phase between the modeled and observed data at far offsets because the initial velocity is not accurate enough. Using the entire offset range would, hence, affect the quality of the estimated wavelet. Therefore, offset-based weights are applied to the data wherein the direct arrivals until 400 m are used in their entirety. The weights are then smoothly tapered to zero over an offset of 800 m, and no data beyond 1200 m are included to estimate the wavelet. These specific values were obtained after several iterations of trial and error estimating the wavelet, comparing the observed data with those generated from the wavelet, and observing the wavelet spectrum. Finally, we ensure that the source-time function (Figure 4c) is causal and goes to zero after the main arrivals by applying cosine tapers. By including a free surface while generating data for source inversion, the inverted source-time function is free of the source ghost.

The spectrum of the weighted modeled data matches that of the source-time function closely (compare Figure 4d and 4h). The relatively larger amplitudes at lower frequencies in the observed data (Figure 4g) could be due to the presence of noise. In addition, the data in this specific case were modeled for nonattenuative media, whereas the recorded wavefield propagated through gas, which could also be responsible for the higher amplitudes. We note that the inversion results are influenced very heavily by the source-time function, and it is worth spending effort to compute a satisfactory wavelet.

During FWI, the same inner mute as the one used during the source estimation is used to remove the Schölte waves in the data. The offset-based weights are zero to an offset of 150 m, increasing linearly to a value of 1 at 350 m and constant (= 1) thereafter (Figure 4b).

No other processing steps, such as deghosting or demultiples, are applied to the observed data. By implementing a free-surface

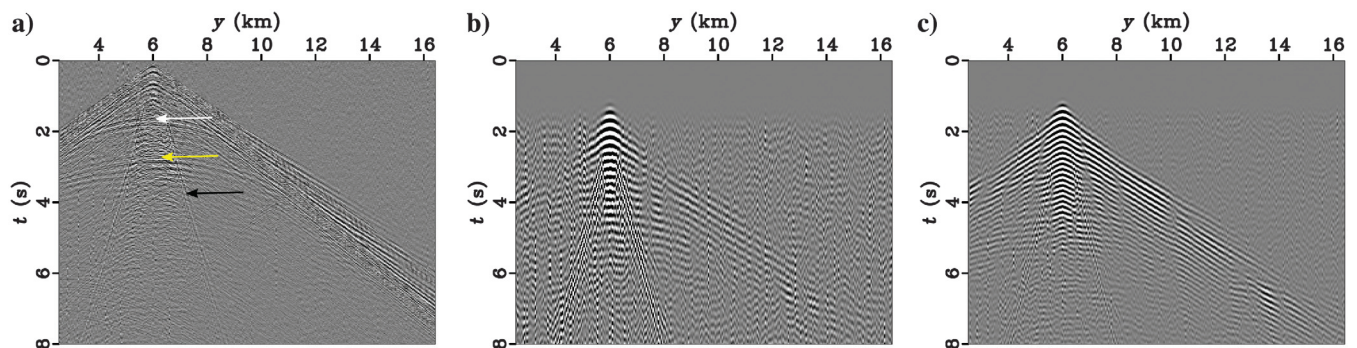


Figure 3. (a) Despiked data along the green-yellow line ($x = 5.46$ km) in Figure 1, recorded at ($x = 5.6$ km, $y = 6.0$ km). The white and yellow arrows indicate reflections from the top of the gas and chalk, respectively, and the black arrow denotes the Schölte waves. The data are filtered between (b) 2.5–5.0 Hz (band 1) and (c) 2.5–7.0 Hz (band 2).

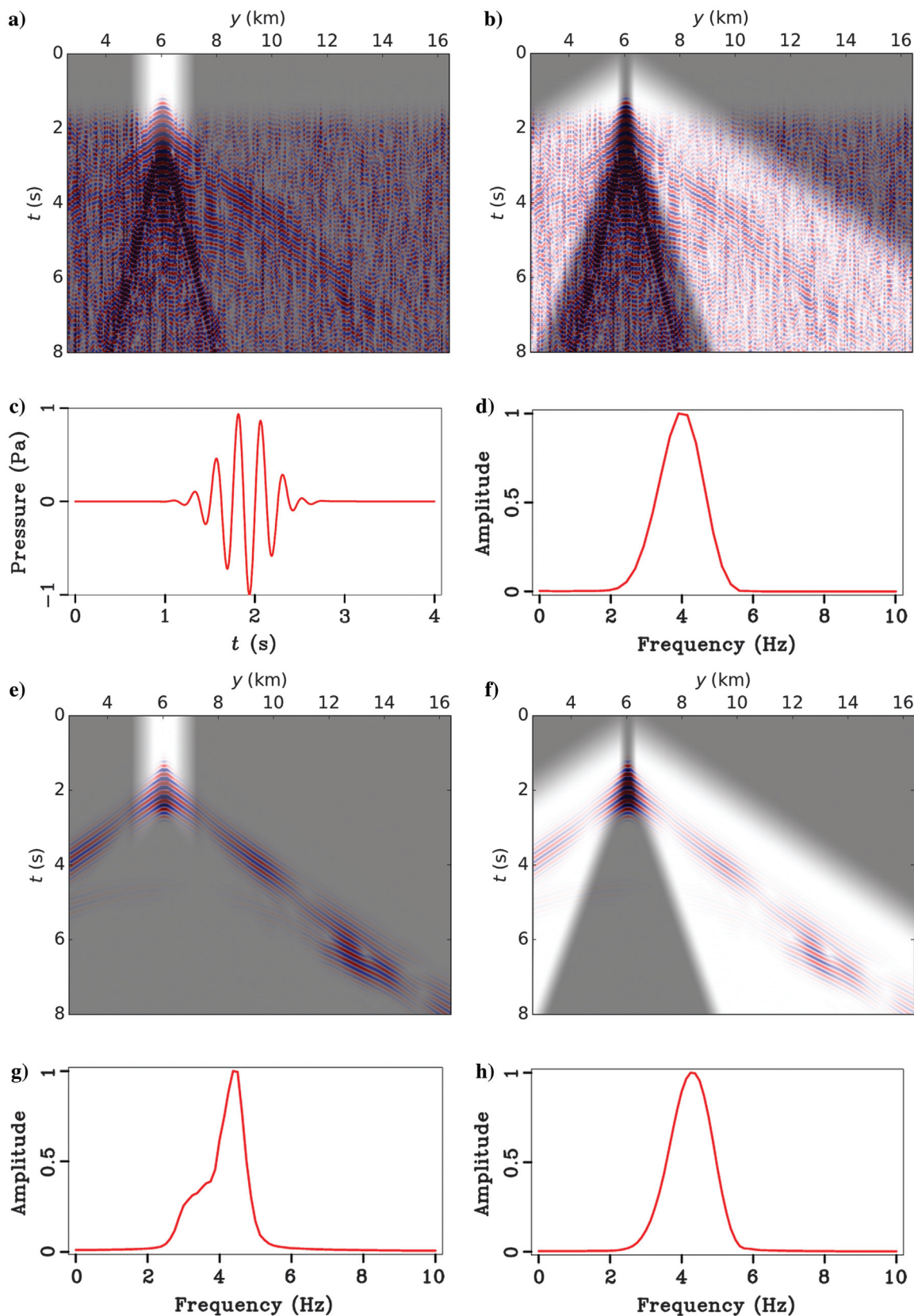


Figure 4. Recorded data in band 1, with data weights for the (a) source inversion and (b) FWI superimposed on them. (c) The source estimated for band 1 by modeling the wavefield in nonattenuative media, and (d) its normalized spectrum. The data modeled with the estimated wavelet in the initial velocity field with weights used for (e) source inversion and (f) FWI overlay on top. The normalized spectra of the weighted (g) observed and (h) modeled data used in FWI.

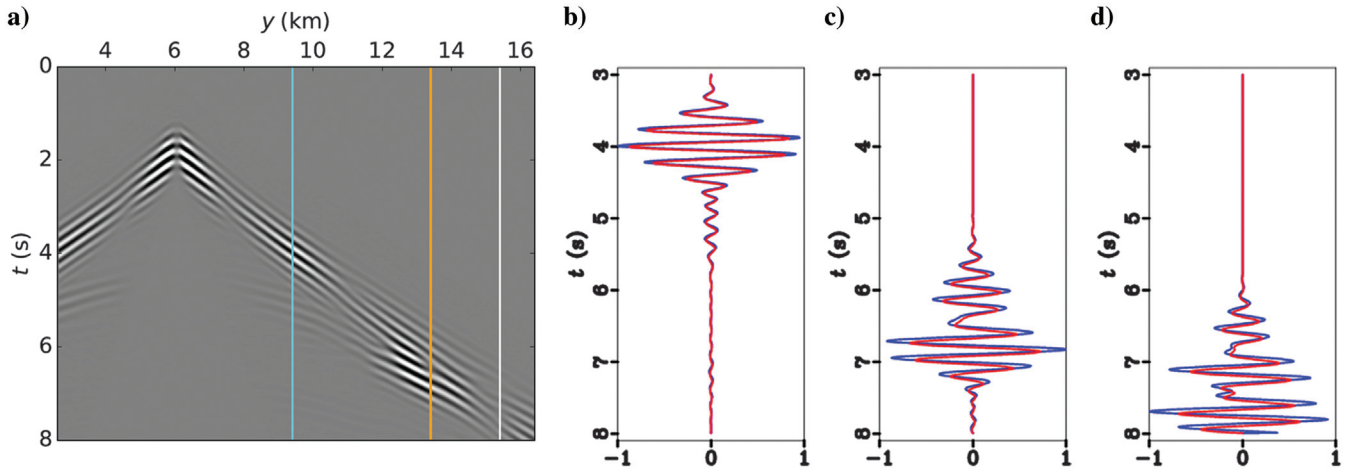


Figure 5. (a) Data in the 2.5–5 Hz range modeled with the initial V_{P0} with attenuation taken into account. A comparison of normalized data modeled with (red) and without (blue) attenuation at offsets of approximately (b) 3.4 km, (c) 7.4 km, and (d) 9.4 km indicated by the cyan, orange, and white lines, respectively, on Figure 5a.

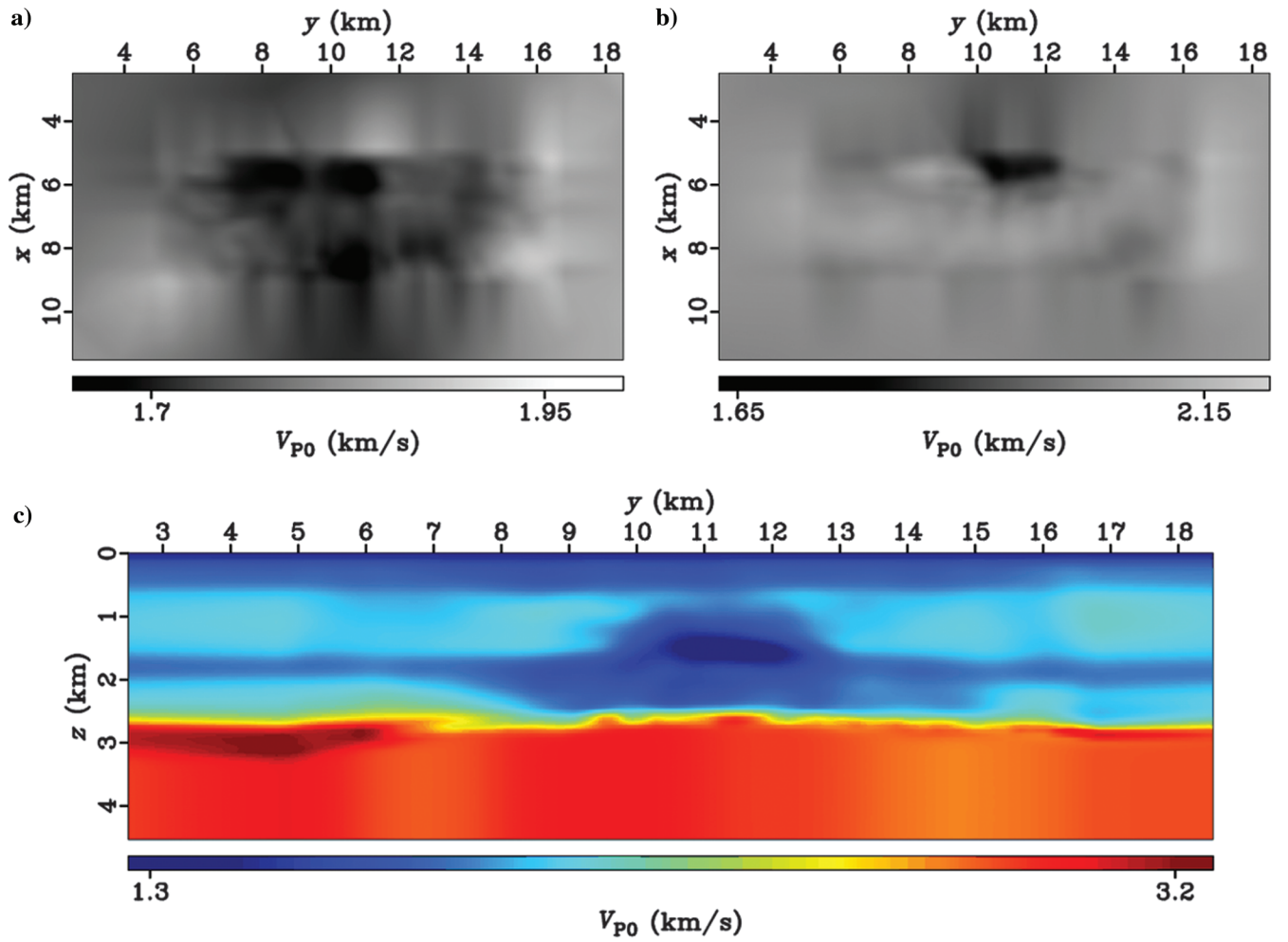


Figure 6. Initial velocity V_{P0} at depths of (a) 0.2 km and (b) 1.0 km, and at (c) $x = 5.6$ km.

condition in the modeling stage, the ghost and surface-related multiples are included in the generated data.

The data subsampling technique adopted during the inversion is similar to the one described in Warner et al. (2013). The 2048 gathers are divided into 16 groups of 128 randomly selected gathers without repetition, and we run three iterations of l-BFGS on each group. The potential gain from running more iterations could be offset by the artifacts introduced because of the sparse sampling of the receiver gathers. The number of iterations chosen per group

is the minimum necessary to benefit from l-BFGS. The number of groups and gathers per group chosen are such that, at the end of a run of inversion, all data are included.

FWI RESULTS

Band 1 (2.5–5.0 Hz)

As stated previously, the tertiary gas-bearing sediments in the Valhall field make the medium attenuative. We compare data

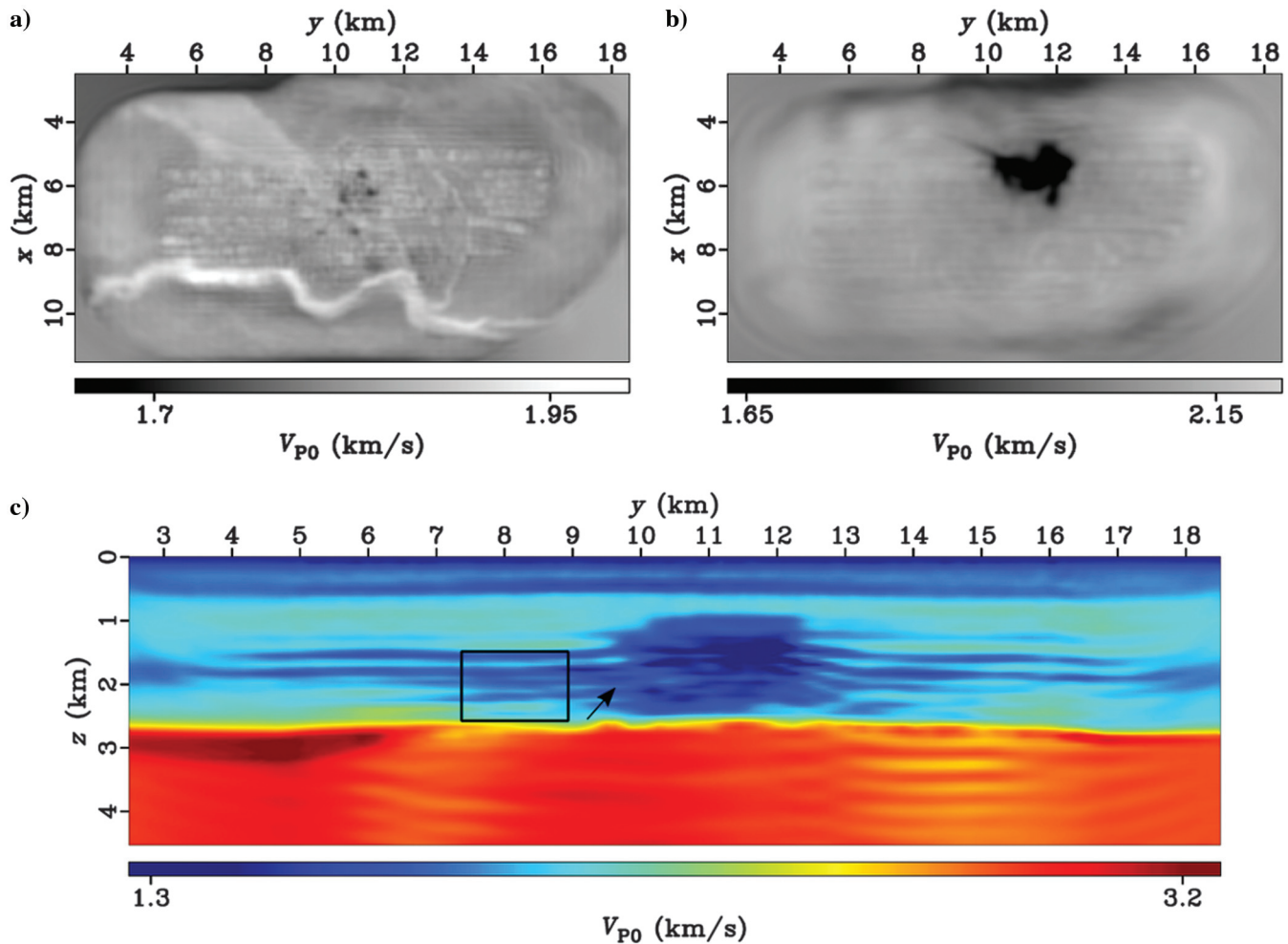
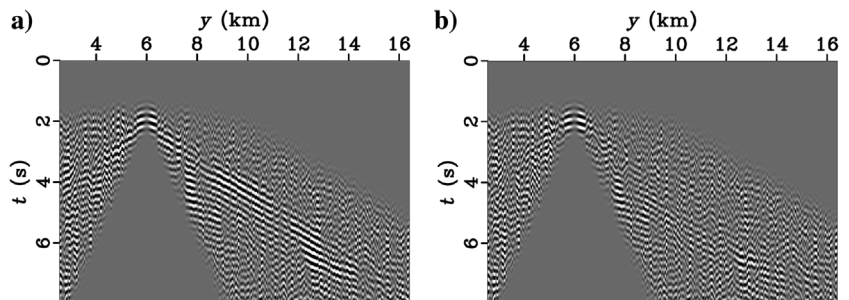


Figure 7. Velocity V_{P0} obtained assuming the medium to be purely acoustic, using data in the 2.5–5.0 Hz frequency range, at (a) $z = 0.2$ km, (b) $z = 1.0$ km, and (c) $x = 6.5$ km. The arrow and box indicate artifacts in the reconstructed velocity because attenuation has not been taken into account.

Figure 8. The difference between observed data and those modeled with (a) the initial V_{P0} and (b) the reconstructed velocity for the wavefield computed in attenuative media.



(the red and blue curves, respectively, in Figure 5b–5d) modeled in the initial velocity field without and with attenuation using a constant- Q model below the water layer (the Q model described previously). Viscosity in the medium causes a decrease in the wavefield amplitudes and, in addition, dispersion delays arrivals of events.

These effects are stronger at larger offsets (compare Figure 5b and 5d).

To study the influence of viscosity on the inversion, we first run FWI without taking attenuation into account. The source-time function (Figure 4c) is estimated from the initial velocity model, and we

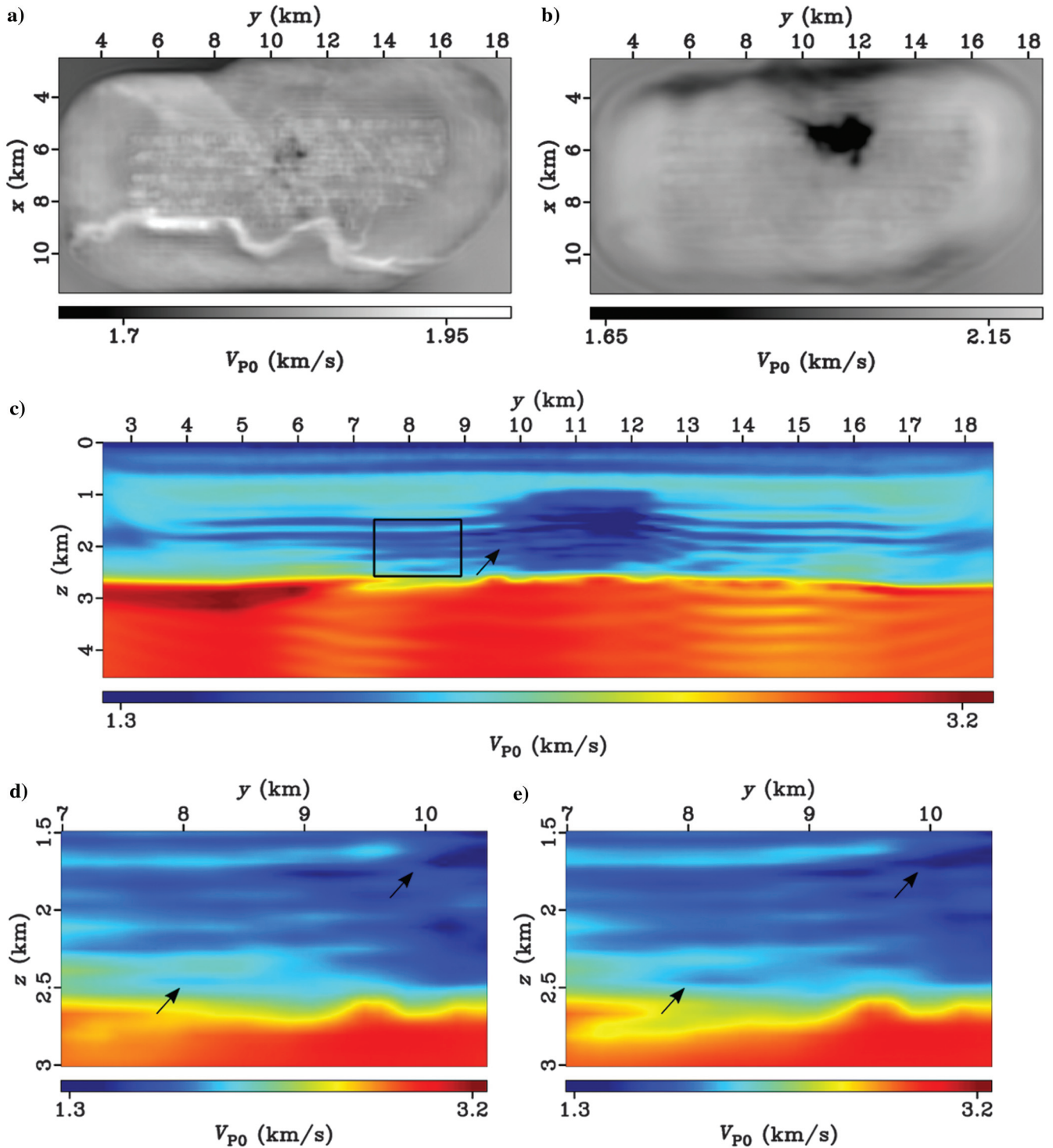


Figure 9. Velocity obtained from V_{P0} -only FWI in viscoacoustic media at depths of (a) 0.2 km and (b) 1.0 km, and at (c) $x = 5.6$ km. Magnified regions at $x = 5.6$ km for (d) nonattenuative FWI (Figure 7) and (f) V_{P0} -only viscoacoustic FWI. The arrows and box indicate a decrease in artifacts when attenuation is taken into account during inversion.

run 16 iterations of l-BFGS. Although the frequencies in the data are limited to 5.0 Hz, significant details emerge in the updated velocities down to a depth of 2.5 km. The underground channels are clearly visible at $z = 0.2$ km (compare Figures 6a and 7a). The velocity inversion at $z \approx 0.6$ km is delineated, as is the top

of the low-velocity region indicative of gas ($z = 1.0$ km), in the vertical section at $x = 5.6$ km (Figure 7c).

Next, FWI is performed assuming the medium to be viscous. We start with the constant- Q model and update only the velocity V_{P0} . For the range of frequencies in the data, the final data misfit for viscoacoustic FWI (Figure 8b) is very close to that for acoustic FWI. However, the model updates that lead to the data misfits are understandably different: the kinematic velocity obtained at 4.0 Hz at $x = 5.6$ km (Figure 9c) has more continuous features (indicated by the black rectangles) than that for acoustic FWI (Figure 7c), although the improvement is not very obvious in the depth slices here. The vertical section shows a decrease in artifacts (the black arrows), improvement in resolution, and an upward shift in events in the low-velocity region as well as in those in the reservoir. As mentioned previously, diving waves do not penetrate the medium deeper than ≈ 1.5 km and the updates are primarily due to FWI operating in the least-squares migration mode.

Simultaneous inversion of V_{P0} and attenuation yields velocities that are very close to those obtained from V_{P0} -only inversion. The updates in Q are also very small: of the order of ± 20 for an initial model that has a constant value of 200 in the sediments. As expected, the difference in the data misfit computed for the final models (V_{P0} -only with Q as a passive parameter, and joint inversion) is insignificant. This is most likely because, at such low frequencies, the objective

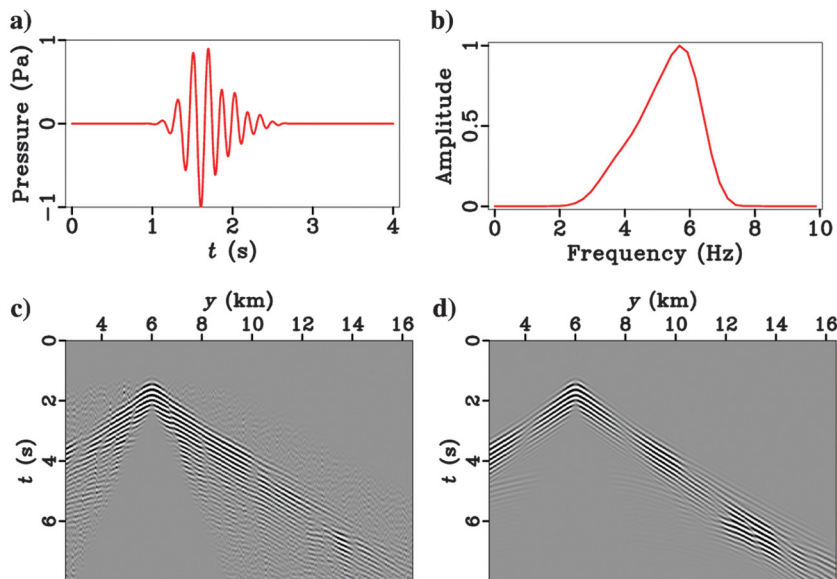


Figure 10. (a) Source-time function and (b) its normalized spectrum computed from (c) the observed data filtered between 2.5 and 7.0 Hz, by modeling the wavefield without taking attenuation into account. (d) The data modeled with the computed wavelet and the initial V_{P0} .

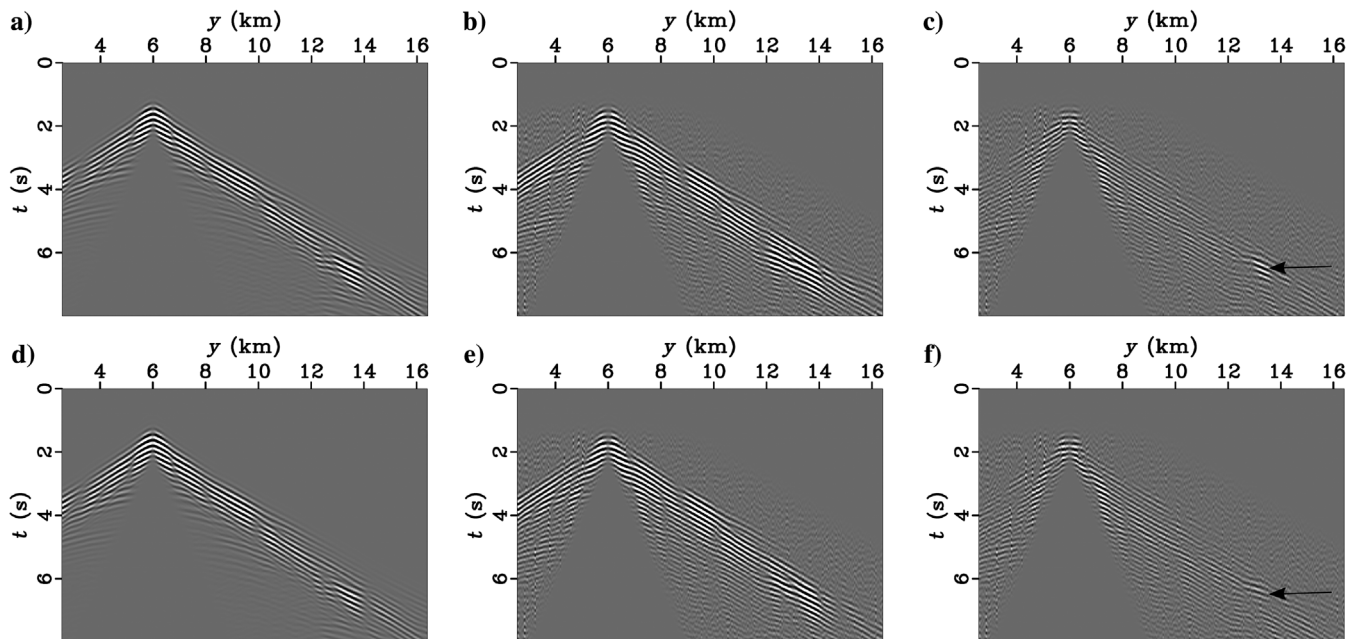


Figure 11. Modeled data and misfit at ($x = 5.6$ km, $y = 6.0$ km), in the 2.5–7.0 Hz frequency range. (a) The data modeled with the velocity obtained from nonattenuative FWI, and the (b) initial and (c) final data misfit. (d) The data computed from the V_{P0} and Q values from their simultaneous inversion, and the (e) initial and (f) final data differences. The arrows indicate differences in the final data misfit for nonattenuative and viscoacoustic FWI.

function is not very sensitive to attenuation. To test that this is indeed the case, we used the velocity-field obtained from the V_{P0} -only inversion as the initial model to run another set of 48 iterations of FWI in the first frequency band to update only the parameter Q . The inversion turned out to be unstable, with the Q -field being assigned erratic and geologically unrealistic values as high as 1000 in the subsurface.

Table 1. Objective function computed for 128 evenly spaced receiver gathers with the respective initial and final models in the two frequency bands.

FWI	Band 1		Band 2	
	Initial misfit	Final misfit	Initial misfit	Final misfit
Without Q	1065	665	65,880	51,430
V_{P0} -only with Q	1095	670	49,900	41,470
V_{P0} - Q simultaneous	1095	665	50,475	41,660

Band 2 (2.5–7.0 Hz)

The output of the inversions from the first frequency band is used to estimate the source-time functions from observed data filtered between 2.5 and 7.0 Hz (Figure 10). We run 48 iterations of FWI for the acoustic, V_{P0} -only viscoacoustic, and joint inversion (V_{P0} - Q).

The influence of attenuation on the inversion is higher for data in the 2.5–7.0 Hz frequency range. There is a larger decrease in the data misfit (qualitatively, as indicated by the arrows in Figure 11, and quantitatively, by Table 1) after inversion when Q , as an active or passive parameter, is taken into account. This is especially noticeable for the reflection from the top of the reservoir: in band 1, the final data misfit with and without attenuation is comparable. However, because higher frequencies are included, inversion using acoustic modeling is unable to steer the velocity to reduce the differences in amplitude. Consequently, the differences in the reconstructed velocities are starker: at shallow depths ($z = 0.2$ km), the acquisition footprint in V_{P0} from nonattenuative FWI is larger, as is noticeable in the depth slices (Figures 12a and 13a) and pointed out by the arrows at depths of ≈ 0.2 km in the sections at $x = 5.6$ km (Figures 12c and 13c).

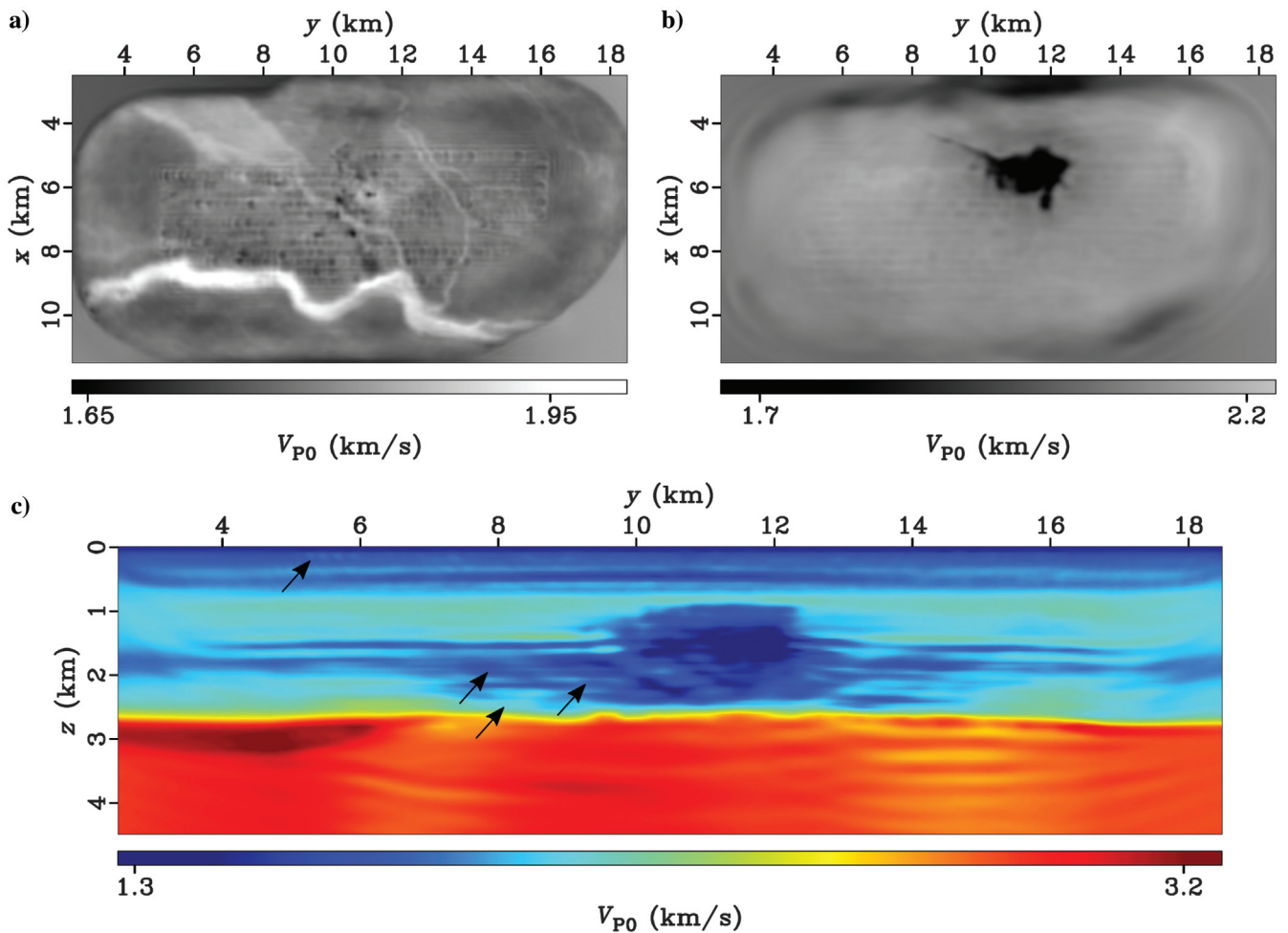


Figure 12. Velocity obtained from FWI of data in the 2.5–7.0 Hz range, assuming the medium is nonattenuative, at depths of (a) 0.2 km, (b) 1.0 km, and at (c) $x = 5.6$ km. The arrows highlight artifacts in the final result.

For depths between 2.0 and 2.5 km, the events in velocity reconstructed from viscoacoustic FWI are more continuous and some diagonal artifacts are mitigated (indicated by the arrows at $2.0 \text{ km} < z < 2.5 \text{ km}$ in Figures 12c and 13c). Wavefields that propagate through the gas cloud experience stronger changes in amplitude and phase compared to those that travel through other wavepaths. When the background values of Q are inaccurate, the distortions in phase and amplitudes are attributed either entirely to velocity updates (in the case of nonattenuative or V_{P0} -only FWI) or disproportionately to them (during V_{P0} - Q -inversion) because of larger sensitivity of the objective function to the parameter V_{P0} . In addition, because FWI without attenuation has to compensate for the viscosity of the medium, it yields velocities that are lower, on average, than the kinematic velocity (computed at 5.5 Hz), which is expected.

It is important to note that the figures displaying velocities reconstructed from viscoacoustic FWI refer to the kinematic velocity. This is the apparent velocity for a given dominant frequency, which allows us to make a fair comparison between the different results. At the low frequencies used in the study, the difference between the kinematic velocities computed for 4.0 and 5.5 Hz are very small: the mean difference between the kinematic velocities computed

for the two frequencies using the initial velocity model is approximately 1.7 m/s. However, to put this in perspective, the mean difference between the initial velocity at infinite frequency and at 4 Hz is nearly 13.9 m/s.

The differences in the final data misfit when performing inversion with Q as an active or passive parameter are extremely small. The kinematic velocity obtained from V_{P0} -only inversion (not shown here) is consequently very close to that from simultaneous FWI of velocity and Q (Figure 13a–13c). The small differences, visible in blinking displays, correlate with the reconstructed values of the attenuation factor (Figure 14): the inverted kinematic velocity from simultaneous inversion is lower (or higher) than that from V_{P0} -only FWI when the values of Q exceed (or are less than) 200. There is a decrease in velocity and Q at shallow depths ($\approx 0.5 \text{ km}$); hence, it is difficult to conclude if the two parameters are well decoupled at these depths and in this frequency band.

Data comparison

The data for the initial and inverted models are generated with the respective wavelets (acoustic, velocity-only viscoacoustic, and V_{P0} - Q simultaneous inversion) computed at the beginning of the inver-

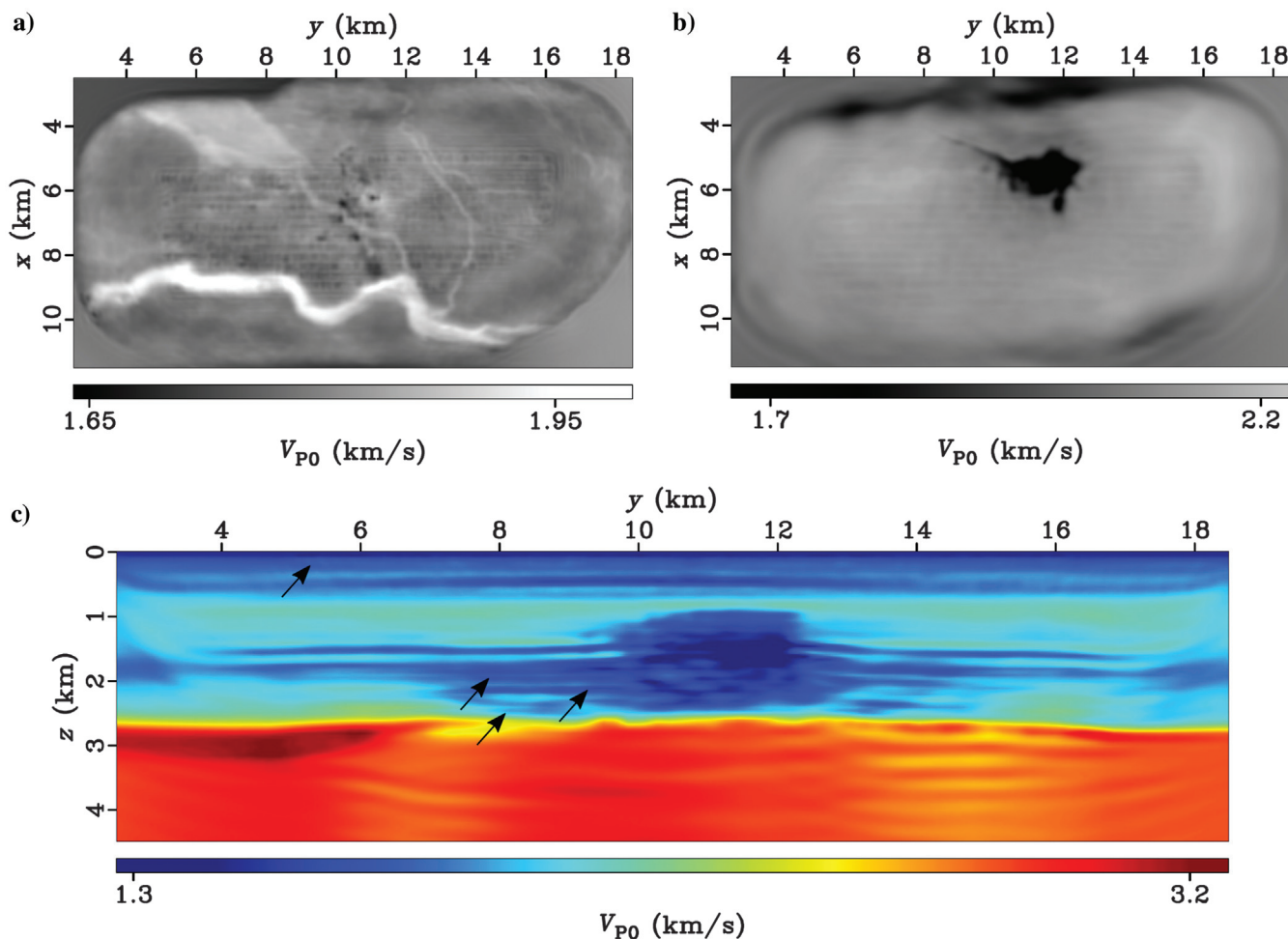


Figure 13. Reconstructed kinematic velocity (at 5.5 Hz) from V_{P0} - Q simultaneous FWI of data in the 2.5–7.0 Hz range, at (a) $z = 0.2 \text{ km}$, (b) $z = 1.0 \text{ km}$, and (c) $x = 5.6 \text{ km}$. The arrows show regions where artifacts decrease because attenuation is taken into account.

sion for band 2. The observed data are plotted in red, white, and blue, whereas those generated with the different models are superimposed in gray scale (Figure 15). The same percentile clip has been applied to each set of data. Less blue-colored events highlighted in the overlaid images indicate a better data match. The data comparisons for V_{p0} -only FWI in the presence of attenuation are not shown because they closely resemble those for the V_{p0} - Q joint inversion.

In the acoustic and viscoacoustic inversions, the data modeled with the initial, as well as the inverted, velocities match the observed ones at near offsets. This is expected because offsets of up to 400 m are used to compute the source-time function. Source wavelets computed with the updated models in the manner described in the “Data Processing and Experimental Setup” section are identical to those used for the inversion. This confirms that the data weights chosen to estimate the wavelet are appropriate and our wavelet estimation is quite robust.

There is significant improvement in the data match for the direct arrivals and diving waves, as seen from the presence of the predominantly red-colored events in Figure 15b and 15d. The fact that the reflections from the top of the reservoir follow the observed data closely gives us confidence in the velocity updates in the top 2.5 km. In addition, the details added to the velocity-field lead to reflections from the top of the gas. There are subtle improvements

in the data fit when the quality factor, as an active or passive parameter, is included in the FWI (indicated by the less blue-colored events in the white boxes in Figure 15d compared to Figure 15b). We also note that the rms value of the final data misfit is lower in the former cases. The impact of Q , however, is more visible in the reconstructed velocities and the obtained images.

Objective function

A quantitative estimate of the objective function gives us some insight into the different types of FWI performed. We use every 16th receiver gather (i.e., a total of 128 gathers) to compute the cost function for the initial and reconstructed models in each frequency band. When data in the 2.5–5.0 Hz are inverted, the initial and final values of the objective functions are very close to each other (Table 1). However, as shown previously, the velocity field reconstructed without attenuation has artifacts in it. Interestingly, the objective function computed for data in the 2.5–7.0 Hz range from the model obtained from the previous band is much higher when the medium is considered to be purely acoustic. This is because the influence of attenuation is larger because we include higher frequencies. Although the decrease in the misfit in this case is also larger compared to V_{p0} -only and V_{p0} - Q simultaneous inversion, the values of the final cost func-

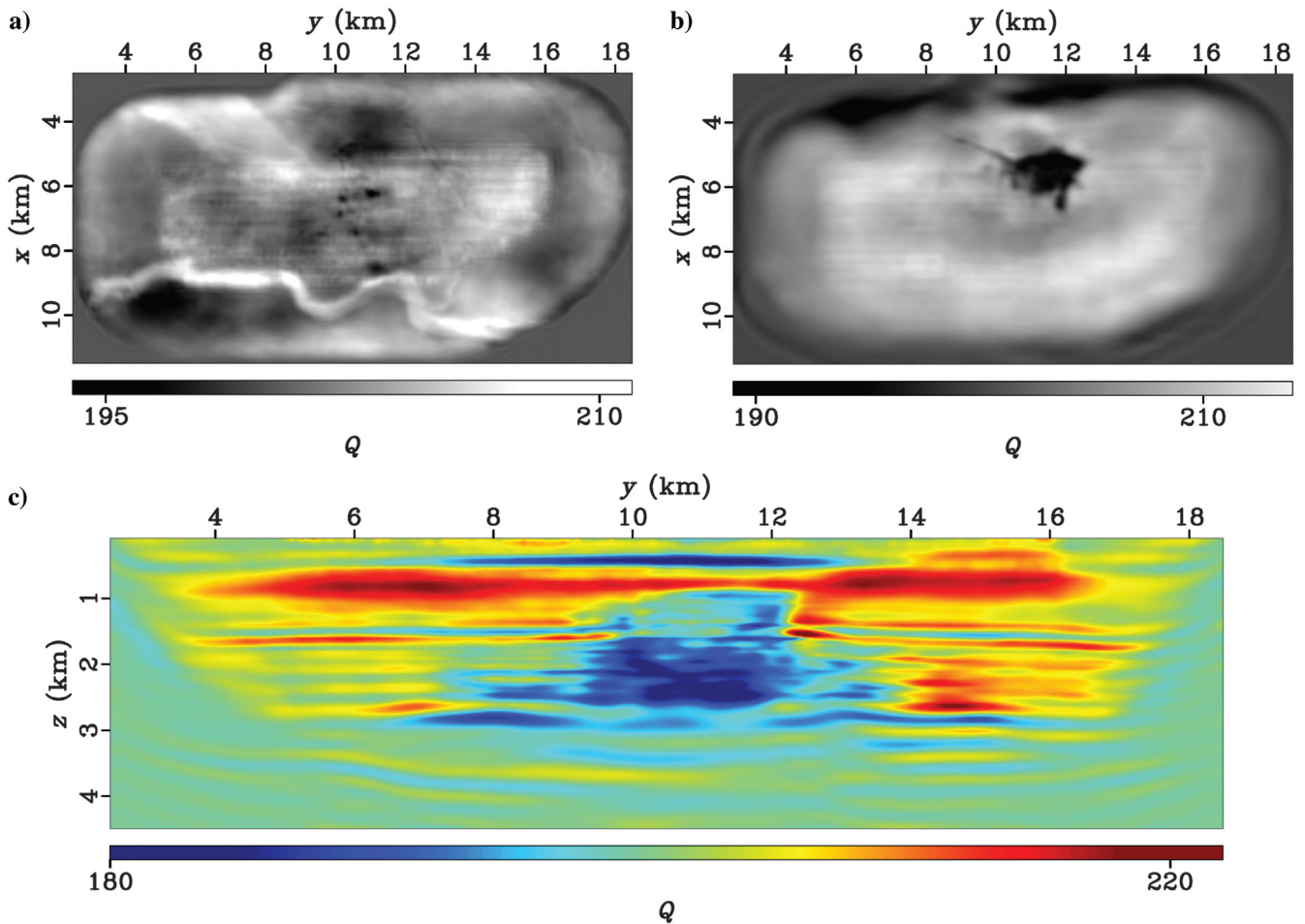


Figure 14. Values of Q at depths of (a) 0.2 km, (b) 1.0 km, and at (c) $x = 5.6$ km, derived from simultaneous (V_{p0} - Q) inversion of data in the 2.5–7.0 Hz range.

tion are lower in the two latter cases. This is obviously the result of incorporating Q as a parameter (active or passive) into the inversion.

Well logs

We have access to logs obtained from three wells in the survey: a deviated well close to the low-velocity anomaly, 2/8-A-3B (referred to henceforth as Log 1); a deviated development well at the northern edge of the survey, 2/8-N-12 (Log 2); and a vertical exploration well 2/11-1 (log 3). The horizontal and vertical coordinates (corresponding to the true vertical depth) from the log files are used to interpolate and extract the initial and inverted velocities from the velocity cubes. The velocities from viscoacoustic FWI correspond to the unrelaxed modulus here and not the kinematic velocity shown in the slices from the model. Once again, we plot only the results from V_{p0} - Q simultaneous inversion; those from V_{p0} -only FWI with Q as a passive parameter are very similar to the former.

The initial and reconstructed velocities at log 1 (Figure 16a) stand out because they are much lower than those estimated by the sonde. The sources and receivers in a sonic log are very close to each other; hence, the velocity obtained from the log is more representative of the formation velocity. The V_{p0} obtained from FWI, however, is over seismic scales and influenced by the low velocities of the gas-bearing sediments in the overburden, which results in slower values compared to the ones from the well log. In addition, the inverted V_{p0} from nonattenuative FWI (the blue curve in Figure 16a) is slower than those from the viscoacoustic inversion because it has to compensate for the phase shifts caused by the viscosity of the medium.

In log 2 (Figure 16b), which is closer to the northwestern edge of the survey, there is good agreement between the well-log data and the reconstructed velocities. The slow velocity of the initial model increases at shallow depths, for $0.8 \text{ km} < z < 1.2 \text{ km}$, especially when attenuation is taken into account. There is also a significant

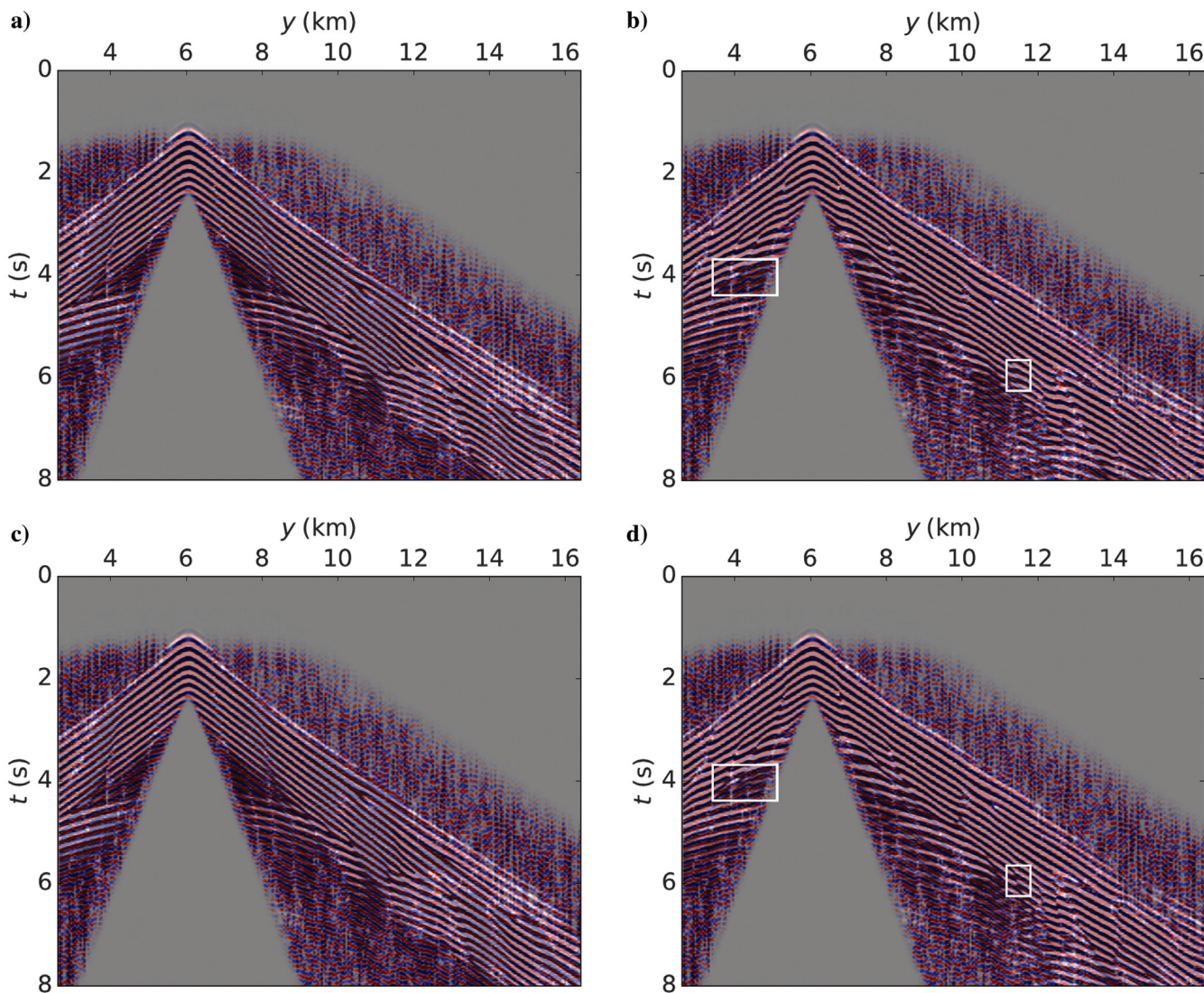


Figure 15. Data (2.5–7.0 Hz) generated with the (a) initial and (b) inverted velocity without taking attenuation into account, overlaid on the recorded pressure component. The data modeled with the (c) initial and (d) inverted parameters V_{p0} and Q when they are updated simultaneously. The boxes indicate regions where the data-match is different for FWI with and without attenuation.

increase of velocity for $1.9 \text{ km} < z < 2.3 \text{ km}$, matching it with the values obtained from the log. There are distinct jumps in the well-log measurements at a depth of 1.5 km, which seems to correspond to an increase in the reconstructed velocity over a distance of $\approx 0.2 \text{ km}$. The computed velocities are, however, underestimated, with respect to the well log, at depths of 0.5 and 0.8 km. Interestingly, this is noticed at Log 3 as well.

At the location of Log 3, the updated velocity profiles match the log measurements at several depths (Figure 16c): for example, at depths of approximately 1.3, 1.55, 1.65, and 1.9 km. As observed

in the other logs, the velocity obtained from nonattenuative FWI is, in general, slower than when Q is taken into account.

Images

The images are computed from the velocity perturbations: the difference between the reconstructed and initial velocity is converted to time, band-pass filtered (1–15 Hz), and then converted back to depth. The artifacts at shallow depths, attributed to the acquisition footprint, and the “diagonal” nongeological artifacts

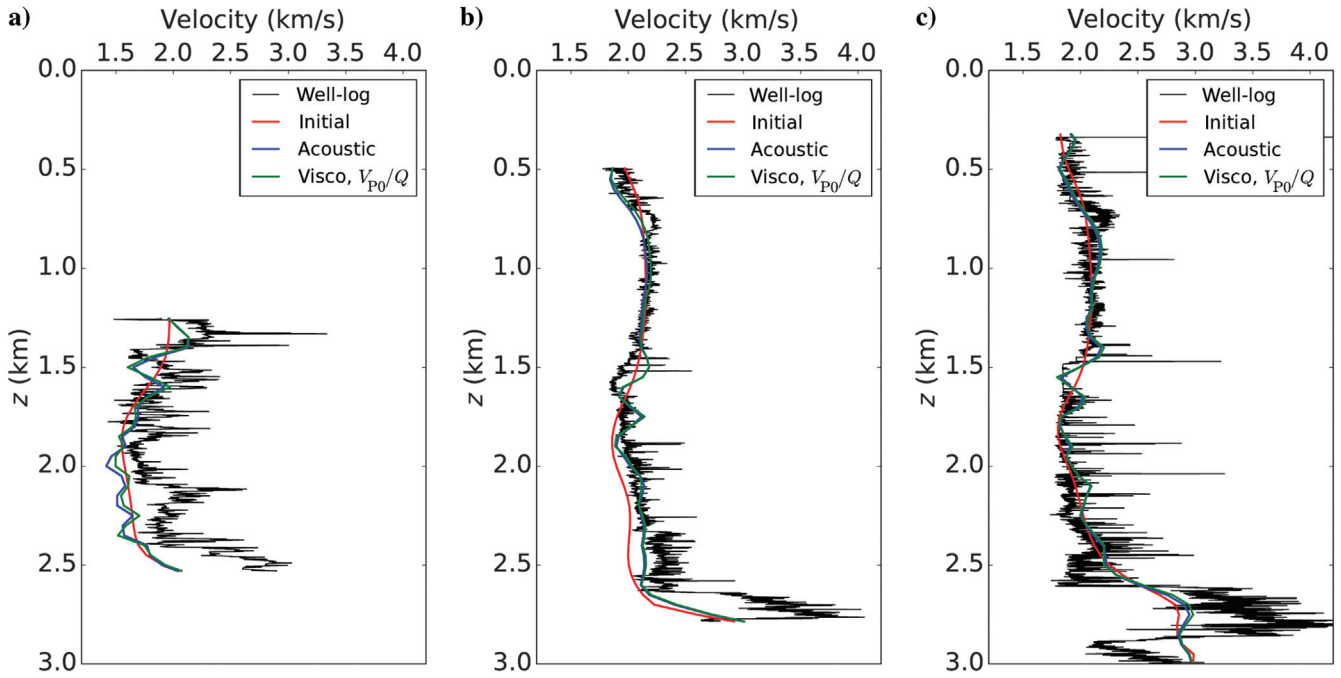


Figure 16. Superposition of well logs from the field over initial velocity and that obtained from FWI in nonattenuative media, and V_{p0} -only and V_{p0} - Q inversion assuming the medium is viscoacoustic. The positions of the logs, (a) Log 1 (2/8-A-3B), (b) Log 2 (2/8-N-12), and (c) Log 3 (2/11-1), are marked in Figure 1.

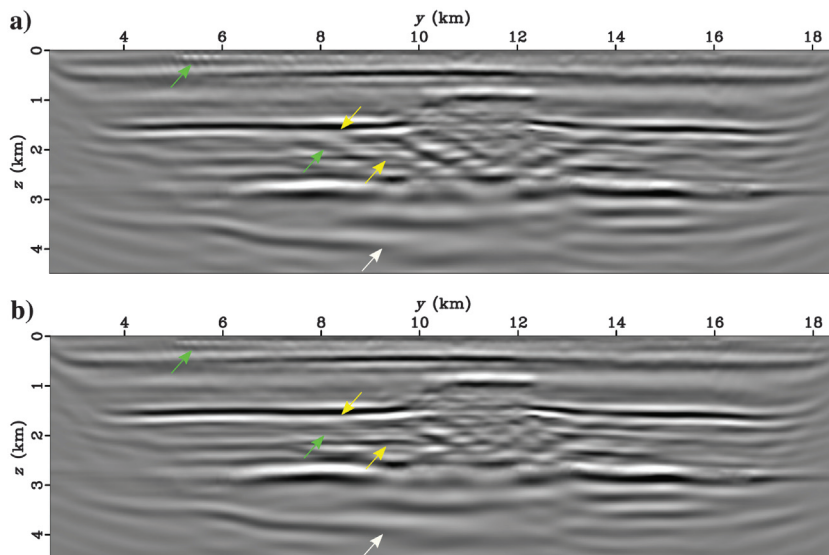


Figure 17. Images computed from the velocities reconstructed from (a) nonattenuative FWI and (b) V_{p0} - Q FWI. The sections in the two cases displayed here correspond to $x = 5.6 \text{ km}$. The arrows indicate differences in the images in two cases.

(shown by the green arrows) are mitigated by viscoacoustic FWI (Figure 17). In addition, the reflectors are more continuous, as indicated by the arrows in yellow. There is significant improvement in the region with the low velocities ($1.0 \text{ km} < z < 2.5 \text{ km}$), in terms of artifacts and the consistency of the events. Taking attenuation into account also shifts some of the deeper reflectors upward: for instance, the one to which the white arrow points. We expect reverse-time migration on the broadband data, which would result in higher wavenumbers in the image, to better highlight the differences.

Computational cost

All of our inversions are run on the Turing IBM Blue Gene/Q machine, access to which is provided by the Institute for Development and Resources in Intensive Scientific Computing (IDRIS). Each compute node consists of 16 cores (16 GB of memory), each of which has a clock speed of 1.6 GHz and can run four threads simultaneously (the hyperthreading functionality). We parallelize over receiver gathers, with two being run simultaneously on each node for both frequency bands in the case of acoustic FWI. To run the inversion in viscoacoustic media, we were able to assign two gathers per node for the first frequency band, but only one per node for band 2. The maximum number of checkpoints permitted by memory (20 and 10 for the first and second bands, respectively) was used. For computing the wavefield for each gather, we take advantage of OpenMP and hyperthreading: 32 or 64 threads are used per receiver gather, depending on the number of gathers processed per node.

The computation time saved per gradient by the CARFS technique relative to conventional checkpointing is 12% and 26%, respectively, for frequency bands 1 and 2. Viscoacoustic FWI of data containing frequencies to 5 Hz requires approximately 28 hours (equivalent to 29,000 scalar hours) to run 48 iterations. This amounts to almost four times the number of hours consumed by acoustic FWI (Table 2). The total number of scalar hours required for inverting data in the second frequency band without and with attenuation is, respectively, 24,500 and 106,500.

DISCUSSION

There are minor differences in the values of inverted velocity V_{P0} obtained from V_{P0} -only viscoacoustic and V_{P0} - Q simultaneous inversions. The updates in the quality factor Q are also not very large. This is reflected in the final data misfit from the two inversions, the difference between which is also not very significant. This, however, does not mean that the parameter Q lies in the null space

Table 2. Computational time required for 48 iterations of FWI for frequency bands 1 and 2 with and without taking attenuation into account.

FWI	Compute time	
	Band 1	Band 2
Without Q	7.5 h (8 cores/gather)	24 h (8 cores/gather)
With Q	28 h (8 cores/gather)	52 h (16 cores/gather)

of the FWI. In fact, as shown in [Operto et al. \(2013\)](#), the radiation patterns of the parameters V_{P0} and Q are similar (isotropic). However, while velocity influences reflected- and diving-wave energy in the data equally, the effect of Q is stronger at farther offsets, in transmitted energy and postcritical reflections ([Operto et al., 2013](#)). With a lower signal-to-noise ratio at larger offsets, it becomes difficult for the inversion to make significant updates to Q . This is because, although Q influences the phase and amplitude of the wavefield, it is a second-order effect.

We note that the V_{P0} -field reconstructed in the 2.5–7.0 Hz frequency range by viscoacoustic FWI in this paper and those estimated by [Operto and Miniussi \(2018\)](#) at 7.0 Hz are qualitatively similar for $0.5 \text{ km} < z < 2.5 \text{ km}$. The features recovered by them match the ones in our work, although their model has higher resolution. This could be because of different smoothing parameters chosen for the gradient during inversion. At shallow depths ($z < 0.5 \text{ km}$), some ringing is present in their estimated velocity field, which might be related to the data used for source estimation. There are structural differences at the top of chalk, and they have larger values of V_{P0} deeper than 2.5 km. The differences in the deeper region could be because of the fact that they apply FWI on a different vintage. They received preprocessed data, and they had approximately 250 more receiver gathers, all of which they use every iteration of FWI.

The Q -field reconstructed by [Operto and Miniussi \(2018\)](#) is also structurally similar to the one obtained here from viscoacoustic FWI. This indicates that our inversion updates the quality factor in the correct direction. As in the case of the P-wave vertical velocity, their Q model has higher resolution. The main difference, however, is that the magnitude of the update in their case is much higher: starting from a constant quality factor of 200 in the sediments, they obtain values of Q as low as 55 in the region with the low-velocity anomaly, which is typical of gas-bearing sediments in the North Sea ([Haacke et al., 2019](#)).

The pseudo-Hessian preconditioner used by [Operto and Miniussi \(2018\)](#), in addition to the fact that they use all of the data in every iteration, most likely helps them make larger updates to the quality factor. There are, however, parameters that must be tuned, and they exert significant influence on the final results (FWI4, compared to FWI5, in their paper). As explained in Appendix A, the data subsampling prevents us from applying the same preconditioner; hence, we resort to a modified version of illumination compensation. Other techniques designed to increase the sensitivity of the objective function to quality factor exist. Applying implicit regularization to one of the model parameters, by scaling it, has been shown to improve convergence of the velocity and the quality factor ([Kamei and Pratt, 2013](#)). Alternatively, a misfit function that emphasizes the amplitude of the signal within a time window can also mitigate crosstalk between the reconstructed velocity and the quality factor ([Pan and Innanen, 2019](#); [Pan and Wang, 2020](#)).

The inverted density ρ in [Operto and Miniussi \(2018\)](#) is supposedly reliable at shallow and intermediate depths. More importantly, however, it absorbs the acquisition footprint during inversion, thereby mitigating the footprint in the final V_{P0} field. This is most likely because the density in the parameter combination V_{P0} - ρ , influences near offsets in the data; as a result, the inversion primarily updates the high-wavenumber component of ρ . We implement a different strategy: we choose not to invert for an additional parameter (density) so that the issue of crosstalk between velocity and ρ

does not arise. Instead, we fix the density field at its initial value throughout the inversion (for both bands). In addition, the data in the near offset (up to 150 m) are muted and are not used during FWI. One potential problem with using a density field obtained from Gardner’s relationship is that the ρ values are not very accurate for gas-bearing rocks. Hence, keeping the density fixed at the erroneous values in the gas cloud can lead to inaccuracies in the reconstructed velocities.

Another interesting issue we discovered here was with regard to placement of the grid points of the density model at the water bottom. The seafloor at Valhall is almost constant at 70 m, as mentioned previously. The grid spacing for the models used during FWI for band 1 is 70 m as well. The velocity, anisotropy coefficients, and quality factor have the first grid point in water and the second one (at $z = 70$ m) in the sediment. The discretization of the viscoacoustic wave equations in the stress-velocity formulation (equation 4) results in staggering the density ρ , stiffness coefficients c_{ijkl} , vertical stress component σ_z , and vertical derivative of the vertical particle velocity v_z (i.e., $\partial_z v_z$) by half a grid point with respect to v_z , buoyancy $1/\rho$, and the quantity $\partial_z \sigma_z$. As a consequence, the P-wave vertical velocity V_{p0} , the anisotropy coefficients ϵ and δ , and the quality factor Q can all share the same grid as far as water and sediment are concerned. However, one must decide if the second grid point of the density model should have values corresponding to those in water or in sediment. With the sec-

ond grid point in the sediment, the buoyancy and v_z have errors in them. However, if the second grid point is placed in water, the vertical stress σ_z tends to be inaccurate. The wavelets computed in each case differ in amplitude and phase, which in turn results in a small systemic shift in depth of the inverted velocity model. We choose to place the second grid point of the density model in the sediment because the data misfit with the source wavelet estimated with this model was lower.

For the second frequency band, the grid spacing in the models is 50 m, which is liable to introduce errors because of its inability to simulate the exact water bottom (which is at $z = 70$ m). In addition, because of the staggered grid, it was necessary to determine if only the first or the first two grid points of the density model should be placed in water. The data misfit being lower in the latter case, we chose the first two grid points of ρ to have values of 1000kg/m^3 .

With the time-domain workflow we have created, it should be fairly straightforward to invert data containing higher frequencies (up to 12 or 15 Hz). In addition to adding further details to the velocity field, we expect larger updates in the parameter Q . With the inclusion of higher frequencies, however, the data will contain more events and, hence, one must be careful while designing weights for source estimation. If the source-time function does not represent the direct arrivals accurately enough (either it has too many, or not enough, wiggles), the reconstructed V_{p0} - and Q -fields will exhibit

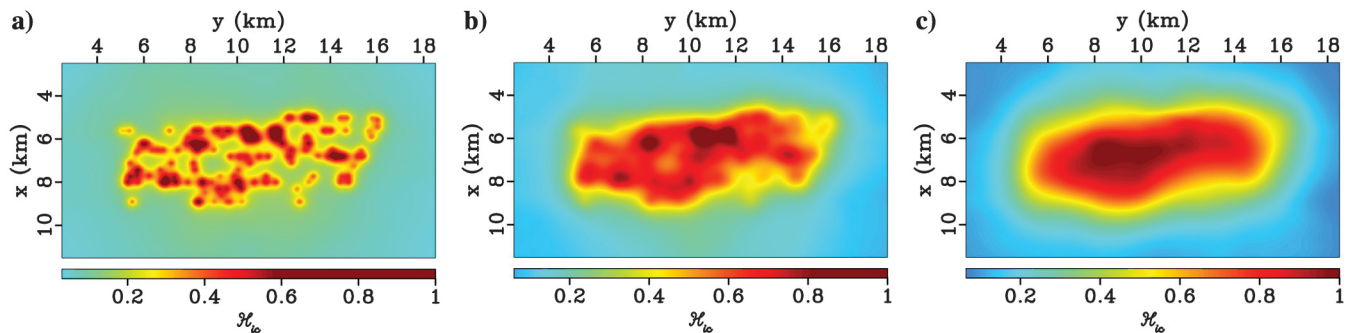


Figure 18. Illumination compensation \mathcal{H}_{ic} at depths of (a) 0.2 km, (b) 0.5 km, and (c) 1.0 km.

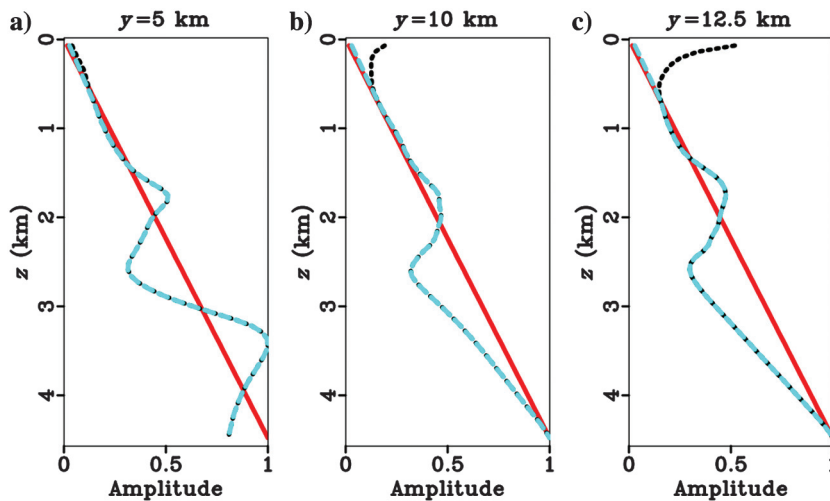


Figure 19. Normalized depth preconditioner amplitude profiles at three locations for a choice of three preconditioners: linear depth preconditioner (red), illumination compensation (black dashed line), and modified illumination compensation (cyan dashed line). The profiles are extracted at $x = 5.6$ km and (a) $y = 5.0$ km, (b) $y = 10.0$ km, and (c) $y = 12.5$ km.

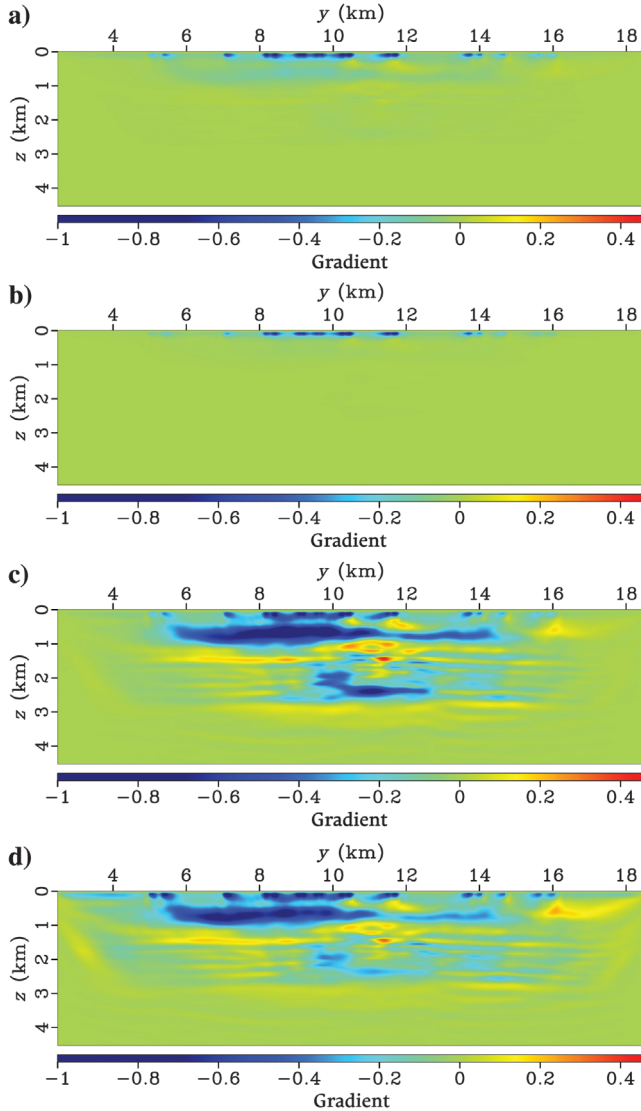


Figure 20. Gradient at $x = 5.6$ km (a) without any preconditioner, (b) with illumination compensation, (c) with depth preconditioning, and (d) modified illumination compensation.

layers that are not indicative of geology but artifacts from the erroneous source wavelet.

We have a data set of a different vintage from the Valhall, which enables time-lapse studies in the area. Several authors have addressed the problem of FWI applied to time-lapse data using different techniques (Asnaashari et al., 2015; Hicks et al., 2016; Yang et al., 2016a). Investigating 4D changes in V_{p0} and Q using an appropriate workflow would be a very interesting problem.

In our study, we use only the pressure data, although we also have three velocity components. The data redundancy resulting from multicomponent data could help constrain the inversion better and aid multiparameter FWI. They also allow for the possibility of investigating viscoelastic FWI, although computationally it is orders of magnitude more expensive than viscoacoustic inversion. This is especially true for low shear-wave velocities at shallow depths because of unconsolidated sediments.

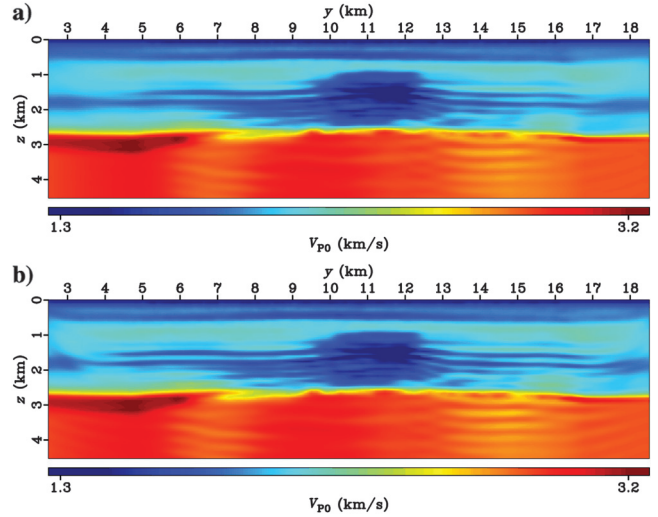


Figure 21. Velocity V_{p0} at $x = 5.6$ km, obtained from viscoacoustic FWI of the 2.5–5.0 Hz data, using (a) depth preconditioning and (b) modified wavefield preconditioning.

CONCLUSION

We perform FWI of a 3D OBC data set from the Valhall field and highlight the differences in the inverted P-wave vertical velocity (V_{p0}) models with and without accounting for attenuation. Time-domain viscoacoustic modeling has lower memory complexity, and better scalability at higher frequencies, compared to its frequency-domain counterpart. Efficiency of time-domain inversion is aided by a data subsampling strategy, resulting in speed-up by a few factors. In addition, we save up to 26% of our computational resources per gradient computation (compared to conventional checkpointing) using the CARFS strategy, when the medium is assumed to be attenuative.

Using even a simple model for the attenuation factor Q (constant values in the subsurface) yields a velocity field that has less geological artifacts than not using any attenuation at all. Although the objective function for the two cases is comparable at lower frequencies, the reconstructed velocity models are understandably different. Because higher frequencies are included in the data, viscoacoustic FWI results in fewer artifacts in the inverted velocity field, in addition to a smaller objective function compared to nonattenuative FWI. Simultaneous inversion of velocity V_{p0} and Q decreases the acquisition footprint in V_{p0} . However, the narrow range of frequencies used in the study is unable to provide reliable updates in the Q -field.

ACKNOWLEDGMENTS

This study was partially funded by the SEISCOPE consortium (<http://seiscope2.osug.fr>), sponsored by Aker BP, CGG, Chevron, Equinor, Exxon-Mobil, JGI, Petrobras, Schlumberger, Shell, Sinopec, and Total. This study was granted access to the HPC resources of the Ciment infrastructure (<https://ciment.ujf-grenoble.fr>) and CINES/IDRIS/TGCC under the allocation 046091 made by Genci. We thank Aker BP ASA and their partner Pandion Energy for providing the data set and permission to present this work, and the help of Ross Milne from Aker BP. We are grateful to S. Operto and J.

Virieux for useful discussions. The comments and feedback of the associate editor, R. Nakata, and three anonymous reviewers helped improve the paper. Figures were generated using the Madagascar package (<http://www.ahay.org>) and Matplotlib.

DATA AND MATERIALS AVAILABILITY

Data associated with this research are confidential and cannot be released.

APPENDIX A

KINEMATIC VELOCITY

A viscous medium causes dispersion and attenuation of the wavefield propagating through it. In the frequency-domain formulation, attenuation is incorporated into the medium by making the velocity field complex-valued (Kolsky, 1956; Futterman, 1962), with the real and complex components being frequency dependent. For a given frequency, the real part of the velocity influences the kinematics of the wavefield, whereas the amplitude depends on the imaginary component. This gives us a way to compare velocities in viscous and nonattenuative media. However, in time-domain modeling, viscous effects are taken into account by using multiple relaxation mechanisms. Hao (2019) shows a way of computing the so-called kinematic velocity.

The stress relaxation function $\psi(t)$ for a generalized SLS body consisting of L mechanisms is (Casula and Carcione, 1992)

$$\psi(t) = M_r \left(1 + \sum_{\ell=1}^L \tilde{Y}_\ell e^{-t/\tau_{\sigma\ell}} \right) H(t), \quad (\text{A-1})$$

where M_r is the relaxed modulus, corresponding to the value of $\psi(t)$ as $t \rightarrow \infty$, \tilde{Y}_ℓ is the anelastic coefficient, $\tau_{\sigma\ell}$ is the stress relaxation time, and $H(t)$ is the Heaviside step function. The anelastic coefficient is expressed in terms of the stress and strain relaxation ($\tau_{\varepsilon\ell}$) times as

$$\tilde{Y}_\ell = \frac{1}{L} \left(\frac{\tau_{\varepsilon\ell}}{\tau_{\sigma\ell}} - 1 \right). \quad (\text{A-2})$$

The unrelaxed modulus M_u , given by $\psi(t)$ for $t \rightarrow 0$, is related to M_r by the relationship

$$M_u = M_r \left(1 + \sum_{\ell=1}^L \tilde{Y}_\ell \right). \quad (\text{A-3})$$

The complex modulus $M(\omega)$ of the system in the frequency domain is

$$M(\omega) = M_r \left(1 + \sum_{\ell=1}^L \frac{\tilde{Y}_\ell i\omega}{\omega_\ell + i\omega} \right), \quad (\text{A-4})$$

where $\omega_\ell (= 2\pi/\tau_{\sigma\ell})$ is the reference frequency for each SLS mechanism. Hao (2019) defines the real part of the complex velocity obtained from equation A-4, for a given peak frequency, as the ‘‘kinematic velocity’’ because it explains the kinematics of the wavefield travelling in viscous media. This is done by first estimating the anelastic coefficients, which are related to the attenuation factor

$Q^{-1}(\omega)$, expressed as the ratio of the imaginary to the real part of the complex modulus $M(\omega)$. Under the assumption of $\tilde{Y}_\ell \ll 1$ (Blanch et al., 1995), $Q^{-1}(\omega)$ reduces to

$$Q^{-1}(\omega) \approx \sum_{\ell=1}^L \tilde{Y}_\ell \frac{\omega\omega_\ell}{\omega^2 + \omega_\ell^2}. \quad (\text{A-5})$$

Instead of solving for each \tilde{Y}_ℓ , Blanch et al. (1995) further assume that the \tilde{Y}_ℓ 's are equal, thereby yielding a linear relationship between the attenuation factor and τ (where $\tau := \tilde{Y}_\ell$). Setting the derivative of the least-squares functional,

$$\int_{\omega_1}^{\omega_2} [Q_0^{-1} - Q^{-1}(\omega, \tau)]^2 d\omega, \quad (\text{A-6})$$

with respect to τ to 0, where Q_0^{-1} is the desired attenuation factor within the frequency range (ω_1, ω_2) , we obtain the value of τ as

$$\tau = \frac{1}{Q_0} \frac{\int_{\omega_1}^{\omega_2} F(\omega) d\omega}{\int_{\omega_1}^{\omega_2} [F(\omega)]^2 d\omega}, \quad (\text{A-7})$$

where

$$F(\omega) = \sum_{\ell=1}^L \frac{\omega\omega_\ell}{\omega^2 + \omega_\ell^2}. \quad (\text{A-8})$$

The unrelaxed modulus M_u , which is the input and output of our modelling and inversion algorithm, is related to the relaxed modulus M_r and τ from the previously mentioned assumption of Blanch et al. (1995) (i.e., $\tau = \tilde{Y}_\ell$) via equation A-3 as

$$M_u = M_r (1 + L\tau). \quad (\text{A-9})$$

The obtained τ and M_r can finally be substituted in equation A-4 to compute the kinematic velocity v_k (Hao, 2019):

$$v_k = \frac{v_r}{\sqrt{2}} \sqrt{\left(1 + \sum_{\ell=1}^L \frac{\tau\omega^2}{\omega^2 + \omega_\ell^2} \right)^2 + \left(\sum_{\ell=1}^L \frac{\tau\omega\omega_\ell}{\omega^2 + \omega_\ell^2} \right)^2 + \left(1 + \sum_{\ell=1}^L \frac{\tau\omega^2}{\omega^2 + \omega_\ell^2} \right)}. \quad (\text{A-10})$$

where v_k is the kinematic velocity and v_r is the velocity corresponding to the relaxed modulus M_r . It can be verified from equations A-9 and A-10 that $v_r < v_k < v_u$, where v_u is the unrelaxed velocity (i.e., the velocity corresponding to the unrelaxed modulus M_u).

APPENDIX B

PRECONDITIONER

For multiparameter FWI, an approximation of the Hessian matrix that takes the scattering pattern of each parameter class into account (Shin et al., 2001; Choi and Shin, 2008) results in better resolution between the different classes. Yang et al. (2018) invert data generated for a synthetic 2D model based on the Valhall field for velocity, density ρ , and the attenuation factor simultaneously by using the pseudo-Hessian as a preconditioner. All three parameters are obtained in Operto and Miniussi (2018) by FWI of 3D OBC data

from the Valhall field by using preconditioned l-BFGS. However, obtaining appropriate values to scale the parameters relative to each other, and damping factors to stabilize the inversion, requires numerous trials. In addition, the 2D synthetic and 3D field studies benefit from regular and sufficient sampling of sources and OBC receivers, respectively. This is not true of the work presented in this paper because of the random data subsampling strategy applied. Hence, in spite of several tests performed to obtain appropriate scaling and damping coefficients, we were not satisfied with the results and resorted to a preconditioner based on illumination compensation.

The illumination-compensation preconditioner applied to the gradient is computed by accumulating (over time) the source wavefield during gradient computation. The preconditioned gradient $\tilde{\mathbf{g}}_p$ is hence given by

$$\mathcal{H}_{ic} = \text{diag} \left[\sum_{\text{shots}} \sum_t |\mathbf{u}|^2 \right]$$

$$\tilde{\mathbf{g}}_p = \mathcal{H}_{ic}^{-1} \mathbf{g}, \quad (\text{B-1})$$

where \mathcal{H}_{ic} is an approximation of the Hessian responsible for illumination compensation, \mathbf{u} is the source wavefield, and \mathbf{g} is the gradient computed from equation 7. The sparse location of the gathers, however, results in nonuniform values of \mathcal{H}_{ic} , especially in the shallow region (Figure 18a). This leads to a preconditioner that has uneven values close to the ocean bottom (the dashed-black plots in Figure 19), resulting in a preconditioned gradient with predominantly larger values at shallow depths (Figure 20b).

We fix this problem by replacing the values of \mathcal{H}_{ic}^{-1} in the shallow region (in this case, depth $z < 800$ m) by a linear function of depth (i.e., z^1). The resulting modified preconditioner (the dashed-cyan plot in Figure 19) has values that are more uniform close to the ocean bottom, thereby yielding gradients that are consistent in depth (Figure 20d). There is significant improvement in the illumination and resolution in the V_{p0} inverted using the modified illumination compensation compared to the depth preconditioning (compare Figure 21a and 21b), along with a corresponding decrease in data misfit.

REFERENCES

- Alkhalifah, T., 1998, Acoustic approximations for processing in transversely isotropic media: *Geophysics*, **63**, 623–631, doi: [10.1190/1.1444361](https://doi.org/10.1190/1.1444361).
- Amestoy, P., R. Brossier, A. Buttari, J.-Y. L'Excellent, T. Mary, L. Métivier, A. Miniussi, and S. Operto, 2016, Fast 3D frequency-domain full waveform inversion with a parallel block low-rank multifrontal direct solver: Application to OBC data from the North Sea: *Geophysics*, **81**, no. 6, R363–R383, doi: [10.1190/geo2016-0052.1](https://doi.org/10.1190/geo2016-0052.1).
- Amestoy, P., R. Brossier, A. Buttari, J.-Y. L'Excellent, T. Mary, L. Métivier, A. Miniussi, S. Operto, J. Virieux, and C. Weisbecker, 2015, 3D frequency-domain seismic modeling with a parallel BLR multifrontal direct solver: 85th Annual International Meeting, SEG, Expanded Abstracts, 3606–3611, doi: [10.1190/segam2015-5811693.1](https://doi.org/10.1190/segam2015-5811693.1).
- Anderson, J. E., L. Tan, and D. Wang, 2012, Time-reversal checkpointing methods for RTM and FWI: *Geophysics*, **77**, no. 4, S93–S103, doi: [10.1190/geo2011-0114.1](https://doi.org/10.1190/geo2011-0114.1).
- Asnaashari, A., R. Brossier, S. Garambois, F. Audebert, P. Thore, and J. Virieux, 2015, Time-lapse seismic imaging using regularized full waveform inversion with prior model: Which strategy?: *Geophysical Prospecting*, **63**, 78–98, doi: [10.1111/1365-2478.12176](https://doi.org/10.1111/1365-2478.12176).
- Barkved, O., A. Bærheim, D. Howe, J. Kommedal, and G. Nicol, 2003, Life of field seismic implementation — Another “First at Valhall”: 65th Annual International Conference and Exhibition, EAGE, Extended Abstracts.
- Blanch, J., J. O. A. Robertson, and W. W. Symes, 1995, Modeling of a constant Q: Methodology and algorithm for an efficient and optimally inexpensive viscoelastic technique: *Geophysics*, **60**, 176–184, doi: [10.1190/1.1443744](https://doi.org/10.1190/1.1443744).
- Brossier, R., S. Operto, and J. Virieux, 2009, Seismic imaging of complex onshore structures by 2D elastic frequency-domain full-waveform inversion: *Geophysics*, **74**, no. 6, WCC105–WCC118, doi: [10.1190/1.3215771](https://doi.org/10.1190/1.3215771).
- Casula, G., and J. Carcione, 1992, Generalized mechanical model analogies of linear viscoelastic behaviour: *Bollettino di Geofisica Teorica ed Applicata*, **XXXIV**, 235–256.
- Cerjan, C., D. Kosloff, R. Kosloff, and M. Reshef, 1985, A nonreflecting boundary condition for discrete acoustic and elastic wave equations: *Geophysics*, **50**, 705–708, doi: [10.1190/1.1441945](https://doi.org/10.1190/1.1441945).
- Choi, Y., and C. Shin, 2008, Frequency-domain elastic full waveform inversion using the new pseudo-Hessian matrix: Experience of elastic Marmousi 2 synthetic data: *Bulletin of the Seismological Society of America*, **98**, 2402–2415, doi: [10.1785/0120070179](https://doi.org/10.1785/0120070179).
- Duveneck, E., and P. M. Bakker, 2011, Stable P-wave modeling for reverse-time migration in tilted TI media: *Geophysics*, **76**, no. 2, S65–S75, doi: [10.1190/1.3533964](https://doi.org/10.1190/1.3533964).
- Futterman, W., 1962, Dispersive body waves: *Journal Geophysical Research*, **67**, 5279–5291, doi: [10.1029/JZ067i013p05279](https://doi.org/10.1029/JZ067i013p05279).
- Gardner, G. F., L. Gardner, and A. Gregory, 1974, Formation velocity and density — The diagnostic basics for stratigraphic traps: *Geophysics*, **39**, 770–780, doi: [10.1190/1.1440465](https://doi.org/10.1190/1.1440465).
- Gholami, Y., R. Brossier, S. Operto, V. Prieux, A. Ribodetti, and J. Virieux, 2013, Which parameterization is suitable for acoustic VTI full waveform inversion? — Part 2: Application to Valhall: *Geophysics*, **78**, no. 2, R107–R124.
- Górszczyk, A., S. Operto, and M. Malinowski, 2017, Toward a robust workflow for deep crustal imaging by FWI of OBS data: The eastern Nankai Trough revisited: *Journal of Geophysical Research, Solid Earth*, **122**, 4601–4630, doi: [10.1002/2016JB013891](https://doi.org/10.1002/2016JB013891).
- Griewank, A., and A. Walther, 2000, Algorithm 799: Revolve: An implementation of checkpointing for the reverse or adjoint mode of computational differentiation: *ACM Transactions on Mathematical Software*, **26**, 19–45, doi: [10.1145/347837.347846](https://doi.org/10.1145/347837.347846).
- Haacke, R., A. Riley-Watson, C. Grimshaw, Z. Dobo, A. King, S. Knapp, C. Schiott, O. Vejbaek, M. Rosengreen, and C. Hidalgo, 2019, Practical multi-parameter FWI at the South Arne field: 81st Annual International Conference and Exhibition, EAGE, Extended Abstracts, doi: [10.3997/2214-4609.201901563](https://doi.org/10.3997/2214-4609.201901563).
- Hall, S., J. Kendall, and O. Barkved, 2002, Fractured reservoir characterization using P-wave AVOA analysis of 3D OBC data: *The Leading Edge*, **21**, 777–781, doi: [10.1190/1.1503183](https://doi.org/10.1190/1.1503183).
- Hao, J., 2019, Seismic imaging: Strategies for visco-acoustic full waveform inversion: Ph.D. thesis, École nationale supérieure des mines de Paris.
- Hicks, E., H. Hoerber, M. Houbiers, S. P. Lescoffit, A. Ratcliffe, and V. Vinje, 2016, Time-lapse full-waveform inversion as a reservoir-monitoring tool — A North Sea case study: *The Leading Edge*, **35**, 850–858, doi: [10.1190/tle35100850.1](https://doi.org/10.1190/tle35100850.1).
- Hicks, G. J., 2002, Arbitrary source and receiver positioning in finite-difference schemes using Kaiser windowed sinc functions: *Geophysics*, **67**, 156–165, doi: [10.1190/1.1451454](https://doi.org/10.1190/1.1451454).
- Kamei, R., and R. G. Pratt, 2013, Inversion strategies for visco-acoustic waveform inversion: *Geophysical Journal International*, **194**, 859–884, doi: [10.1093/gji/ggt109](https://doi.org/10.1093/gji/ggt109).
- Kolsky, H., 1956, The propagation of stress pulses in viscoelastic solids: *Philosophical Magazine*, **1**, 693–710, doi: [10.1080/14786435608238144](https://doi.org/10.1080/14786435608238144).
- Leonard, R., and J. Munns, 1987, Valhall field in geology of Norwegian oil and gas fields: *Graham and Trotman*.
- Li, Y., L. Métivier, R. Brossier, B. Han, and J. Virieux, 2015, 2D and 3D frequency-domain elastic wave modeling in complex media with a parallel iterative solver: *Geophysics*, **80**, no. 3, T101–T118, doi: [10.1190/geo2014-0480.1](https://doi.org/10.1190/geo2014-0480.1).
- Métivier, L., and R. Brossier, 2016, The SEISCOPE optimization toolbox: A large-scale nonlinear optimization library based on reverse communication: *Geophysics*, **81**, no. 2, F11–F25, doi: [10.1190/geo2015-0031.1](https://doi.org/10.1190/geo2015-0031.1).
- Munns, J. W., 1985, The Valhall field: A geological overview: *Marine and Petroleum Geology*, **2**, 23–43, doi: [10.1016/0264-8172\(85\)90046-7](https://doi.org/10.1016/0264-8172(85)90046-7).
- Nocedal, J., 1980, Updating Quasi-Newton matrices with limited storage: *Mathematics of Computation*, **35**, 773–773, doi: [10.1090/S0025-5718-1980-0572855-7](https://doi.org/10.1090/S0025-5718-1980-0572855-7).
- Operto, S., R. Brossier, Y. Gholami, L. Métivier, V. Prieux, A. Ribodetti, and J. Virieux, 2013, A guided tour of multiparameter full waveform inversion for multicomponent data: From theory to practice: *The Leading Edge*, **32**, 1040–1054, doi: [10.1190/tle32091040.1](https://doi.org/10.1190/tle32091040.1).
- Operto, S., and A. Miniussi, 2018, On the role of density and attenuation in 3D multi-parameter visco-acoustic VTI frequency-domain FWI: An OBC case study from the North Sea: *Geophysical Journal International*, **213**, 2037–2059, doi: [10.1093/gji/ggy103](https://doi.org/10.1093/gji/ggy103).
- Operto, S., A. Miniussi, R. Brossier, L. Combe, L. Métivier, V. Monteiller, A. Ribodetti, and J. Virieux, 2015, Efficient 3-D frequency-domain mono-parameter full-waveform inversion of ocean-bottom cable data: Application to Valhall in the visco-acoustic vertical transverse isotropic

- approximation: *Geophysical Journal International*, **202**, 1362–1391, doi: [10.1093/gji/ggv226](https://doi.org/10.1093/gji/ggv226).
- Operto, S., J. Virieux, P. Amestoy, J.-Y. L'Écellent, L. Giraud, and H. Ben Hadj Ali, 2007, 3D finite-difference frequency-domain modeling of visco-acoustic wave propagation using a massively parallel direct solver: A feasibility study: *Geophysics*, **72**, no. 5, SM195–SM211, doi: [10.1190/1.2759835](https://doi.org/10.1190/1.2759835).
- Pan, W., and K. A. Innanen, 2019, Amplitude-based misfit functions in viscoelastic full-waveform inversion applied to walk-away vertical seismic profile data: *Geophysics*, **84**, no. 5, B335–B351, doi: [10.1190/geo2018-0765.1](https://doi.org/10.1190/geo2018-0765.1).
- Pan, W., and Y. Wang, 2020, On the influence of different misfit functions for attenuation estimation in viscoelastic full-waveform inversion: Synthetic study: *Geophysical Journal International*, **221**, 1292–1319, doi: [10.1093/gji/ggaa089](https://doi.org/10.1093/gji/ggaa089).
- Plessix, R. E., 2006, A review of the adjoint-state method for computing the gradient of a functional with geophysical applications: *Geophysical Journal International*, **167**, 495–503, doi: [10.1111/j.1365-246X.2006.02978.x](https://doi.org/10.1111/j.1365-246X.2006.02978.x).
- Plessix, R. E., and C. Perkins, 2010, Full waveform inversion of a deep water ocean bottom seismometer dataset: *First Break*, **28**, 71–78, doi: [10.3997/1365-2397.2010013](https://doi.org/10.3997/1365-2397.2010013).
- Pratt, R. G., 1999, Seismic waveform inversion in the frequency domain — Part I: Theory and verification in a physical scale model: *Geophysics*, **64**, 888–901, doi: [10.1190/1.1444597](https://doi.org/10.1190/1.1444597).
- Pratt, R. G., and R. M. Shipp, 1999, Seismic waveform inversion in the frequency domain, Part II: Fault delineation in sediments using crosshole data: *Geophysics*, **64**, 902–914, doi: [10.1190/1.1444598](https://doi.org/10.1190/1.1444598).
- Prieux, V., R. Brossier, Y. Gholami, S. Operto, J. Virieux, O. Barkved, and J. Kommedal, 2011, On the footprint of anisotropy on isotropic full waveform inversion: The Valhall case study: *Geophysical Journal International*, **187**, 1495–1515, doi: [10.1111/j.1365-246X.2011.05209.x](https://doi.org/10.1111/j.1365-246X.2011.05209.x).
- Prieux, V., R. Brossier, S. Operto, and J. Virieux, 2013, Multiparameter full waveform inversion of multicomponent OBC data from Valhall — Part 1: Imaging compressional wavespeed, density and attenuation: *Geophysical Journal International*, **194**, 1640–1664, doi: [10.1093/gji/ggt177](https://doi.org/10.1093/gji/ggt177).
- Raknes, E. B., B. Arntsen, and W. Weibull, 2015, Three-dimensional elastic full waveform inversion using seismic data from the Sleipner area: *Geophysical Journal International*, **202**, 1877–1894, doi: [10.1093/gji/ggv258](https://doi.org/10.1093/gji/ggv258).
- Shin, C., K. Yoon, K. J. Marfurt, K. Park, D. Yang, H. Y. Lim, S. Chung, and S. Shin, 2001, Efficient calculation of a partial derivative wavefield using reciprocity for seismic imaging and inversion: *Geophysics*, **66**, 1856–1863, doi: [10.1190/1.1487129](https://doi.org/10.1190/1.1487129).
- Sirgue, L., O. I. Barkved, J. Dellinger, J. Etgen, U. Albertin, and J. H. Kommedal, 2010, Full waveform inversion: The next leap forward in imaging at Valhall: *First Break*, **28**, 65–70, doi: [10.3997/1365-2397.2010012](https://doi.org/10.3997/1365-2397.2010012).
- Tarantola, A., 1984, Inversion of seismic reflection data in the acoustic approximation: *Geophysics*, **49**, 1259–1266, doi: [10.1190/1.1441754](https://doi.org/10.1190/1.1441754).
- Warner, M., A. Ratcliffe, T. Nangoo, J. Morgan, A. Umpleby, N. Shah, V. Vinje, I. Stekl, L. Guasch, C. Win, G. Conroy, and A. Bertrand, 2013, Anisotropic 3D full-waveform inversion: *Geophysics*, **78**, no. 2, R59–R80, doi: [10.1190/geo2012-0338.1](https://doi.org/10.1190/geo2012-0338.1).
- Yang, D., F. Liu, S. Morton, A. Malcom, and M. Fehler, 2016a, Time-lapse full-waveform inversion with ocean-bottom-cable data: Application on Valhall field: *Geophysics*, **81**, no. 4, R225–R235, doi: [10.1190/geo2015-0345.1](https://doi.org/10.1190/geo2015-0345.1).
- Yang, P., R. Brossier, L. Métivier, and J. Virieux, 2016b, A review on the systematic formulation of 3D multiparameter full waveform inversion in viscoelastic medium: *Geophysical Journal International*, **207**, 129–149, doi: [10.1093/gji/ggw262](https://doi.org/10.1093/gji/ggw262).
- Yang, P., R. Brossier, L. Métivier, and J. Virieux, 2016c, Wavefield reconstruction in attenuating media: A checkpointing-assisted reverse-forward simulation method: *Geophysics*, **81**, no. 6, R349–R362, doi: [10.1190/geo2016-0082.1](https://doi.org/10.1190/geo2016-0082.1).
- Yang, P., R. Brossier, L. Métivier, J. Virieux, and W. Zhou, 2018, A time-domain preconditioned truncated Newton approach to multiparameter visco-acoustic full waveform inversion: *SIAM Journal on Scientific Computing*, **40**, B1101–B1130, doi: [10.1137/17M1126126](https://doi.org/10.1137/17M1126126).

Biographies and photographs of the authors are not available.